IRON - MANGANESE SULPHIDES

AT HIGH TEMPERATURES

A STUDY OF IRON-MANGANESE SULPHIDES IN IRON AT HIGH TEMPERATURES

By

IAN S. R. CLARK, B.A.Sc.

A Thesis

Submitted to the Faculty of Graduate Studies

in Partial Fulfilment of the Requirements

for the Degree

Master of Engineering

McMaster University

December 1964

MASTER OF ENGINEERING
(Metallurgy)

McMASTER UNIVERSITY
Hamilton, Ontario.

TITLE : A Study of Iron-Manganese Sulphides in Iron at High Temperatures

AUTHOR : Ian S. R. Clark, B.A.Sc. (University of British Columbia)

SUPERVISORS : Professors J. S. Kirkaldy and R. G. Ward

NUMBER OF PAGES : x, 56

SCOPE AND CONTENTS :

This thesis describes a study of the portion of the iron-manganese-sulphur constitution diagram important in steel solidification and ingot soaking (1300°C). Attempts were made to determine a ternary isotherm at 1300°C by microanalysis of samples comprising Mn and FeS contained in and equilibrated with iron pots. A levitation melting technique was used to equilibrate Fe-Mn sulphide and Fe at 1535°C. Diffusion couples between solid Fe - 3.16% Mn and liquid FeS were reacted at 1300°C, quenched and then microanalyzed to determine the stages by which manganese in the iron diffuses to the sulphide phase to produce the βMnS inclusions found in many steels.

Acknowledgements

The author is indebted to Drs. J. S. Kirkaldy and R. G. Ward for introducing the problem and for their continued advice and assistance throughout the course of this study. Thanks are due to Drs. G. R. Purdy and A. McLean and to Mr. J. M. Shapiro for many stimulating discussions. The help of Mr. H. Walker in electron probe microanalysis is also appreciated.

The generosity of Dr. L. Thomasson of the University of Michigan and of Messrs. L. Eaton and F. Jamieson of the Steel Company of Canada is acknowledged for providing some of the materials.

This work was carried out with the financial assistance of the American Iron and Steel Institute through a grant to Dr. J. S. Kirkaldy.

Table of Contents

List of Tables

List of Illustrations

CHAPTER I

Introduction

It has been suggested by Kirkaldy et al[1] that the diffusion of manganese in solid iron toward sulphide inclusions at soaking pit temperatures is responsible for the intermittent ferritic banding frequently associated with fractures in the butt-welds of pipe. Such inclusions are often found distributed within the ferrite bands and manganese impoverishment in the surrounding ferrite has been clearly demonstrated[1] with the electron probe. This intermittent segregation is not to be confused with the intense segregation of carbon that results from the interdendritic segregation of alloying elements during solidification. Kirkaldy et al[2] have shown that such segregation, commonly called "pearlitic banding", results from a delay or advance in the time for initiating ferrite nucleation in high alloy regions. Thus when manganese is the principal alloy element, the A_{e3} line is lowered upon cooling, ferrite nucleation is delayed, and the carbon concentration is increased in manganese-rich regions. Also, the lower activity of carbon in iron in the presence of manganese aids carbon rejection to the high manganese regions where pearlite forms on further cooling. This pearlitic banding will not be considered further because it appears unrelated to the manganese transfer associated with the non-periodic sulphide induced banding.

Until recently it was widely accepted that this intermittent banding was caused by phosphorous segregation, hence, the term "phos-banding" was applied. However, it has been well established[1] by fundamental studies with diffusion couples and by electron probe microanalysis of commercial steels that there is no significant relationship between phosphorous segregation and non-periodic ferrite banding.

The formation of sulphides in steel was simulated in the Fe-Mn-S system at soaking pit temperatures (1300°C) by equilibrating Mn and FeS in Fe containers, while levitation melting was used to equilibrate Fe with Fe-Mn sulphides at 1535°C. Samples produced by these two methods were examined metallographically and then microanalysed by electron probe in an attempt to determine the compositions of αFeS, βMnS and αFe phases. It was found that the Mn/S ratio was important in determining which sulphide phases, αFeS, βMnS, or both, were present in the samples. These experimental results, together with a knowledge of thermodynamics and the bounding binary phase diagrams, permitted a semi-schematic construction of ternary isotherms in the Fe-Mn-S system.

Diffusion couples between solid Fe - 3.16% Mn and liquid FeS showed that manganese diffused from the Fe-Mn phase to the FeS phase, thereby changing the sulphide to two phases, FeS and βMnS. The observed diffusion path when plotted on the ternary isotherm is consistent with the multiphase diffusion theory of Kirkaldy and Brown, which correctly predicts the ferrite precipitates observed in the βMnS phase of commercial steels.

CHAPTER II

Review of Previous Work

This literature review considers the results of research which impart a background knowledge for a study of sulphides in the ternary system Fe-Mn-S. Investigations of inclusions in steels have generally been confined to the study of their effects on mechanical properties and all two frequently no assessment is made of the effects of inclusion composition. Therefore the available phase diagrams are discussed in order to provide a framework which aids the study of solidification and diffusion phenomena.

1. Inclusions in Steel

All commercial steels when examined metallographically are found to contain small nonmetallic particles called inclusions[3,4,5]. These particles may be of widely varying composition, size, shape and distribution and no commercial steel can be made free of them. At best, inclusion compositions can be altered to promote more desirable mechanical properties in the steel. For example, steelmakers have long realized that the addition of manganese encourages the formation of the manganese-rich βMnS phase in either globules or idiomorphic crystals. This type of inclusion has a much higher melting point than does the iron-rich α + β sulphide which otherwise may exist as a thin liquid film around the primary grain boundaries at rolling temperatures.

Sims[3] has classed nonmetallic inclusions in three groups according to origin. The first type are natural or endogenous inclusions which have precipitated from molten or solidifying steel. Inclusions can also enter the bath by erosion of refractories in contact with the flowing steel. Finally, oxidation of the melt by the atmosphere during teeming is also thought to produce inclusions. Although the latter two sources may be of commercial concern, they are of no consequence in this study and only the inclusions precipitated naturally from the melt or solidified iron will be considered further.

The principal natural inclusions are sulphides and oxides but common steel compositions can also lead to phosphides, selenides, nitrides and carbides[3]. The endogenous sulphides, the only inclusions of concern in this study, have been supposed to form in three main ways[3]:

1. By decreasing sulphide solubility as the temperature falls in the liquid steel.
2. By concentration of manganese and sulphur between the dendrites.
3. By decreasing sulphide solubility in solid iron with falling temperature and with phase changes.

The precipitated inclusions are seldom pure or simple compounds and are much more likely to be mixtures[3]. The velocity of reaction and diffusion are thought to control the approach to equilibrium between the sulphide and liquid steel. Thus the composition of small inclusions depends upon the melt composition. Inclusions which

solidify or precipitate after the surrounding steel solidifies will usually assume the shape of droplets or spread along the primary grain boundaries, depending on interfacial tension. But inclusions whose melting points are above the melting temperature of the steel will precipitate as crystals with well-defined faces characteristic of the natural crystalline form of the material. For example, MnS inclusions appear as random sections of octahedra which are in the cubic system.

When sulphides precipitate they can produce different patterns in the primary grain boundaries depending on the elements in the steel. Sims[6] suggests that large globules, few in number and far apart, do not have the characteristics of a eutectic but appear to be formed over a temperature range by progressive rejection of sulphide from solidifying iron, longer freezing times producing larger sulphides. However, some sulphides high in manganese do exhibit a typical eutectic pattern. In this case, Sims speculates that sulphur concentrates in the remaining liquid until a eutectic composition is reached and then freezes at constant temperature.

Sims has further grouped sulphides into three types depending on the degree of deoxidation in the steel[3,4,5,6]. According to this worker, type I inclusions are large, well dispersed, globular sulphides occurring in steels with oxygen contents above 80 to 100 p.p.m.[6,7] and with almost no metallic aluminum residue. Silicon contents over 0.044 per cent are reported to make a negligible change in the sulphide composition. These characteristically spherical type I sulphides, then,

are not pure MnS because the freezing point of this compound is roughly 100°C above the liquidus of the steel. Instead, Sims points out that type I inclusions are likely to be impure manganese sulphides containing iron sulphide and some oxides of manganese, iron and silicon and hence would have freezing points below the solidus temperature of the steel. The implication here is that normally the sulphides form initially as βMnS and no allowance is made for reactions between liquid sulphide and solid iron which may alter the composition of the inclusion.

Below about 80 to 100 p.p.m. of oxygen in the steel the sulphides precipitate as small particles or narrow films in the primary grain boundaries according to Sims[6,7], who calls these type II inclusions. Such inclusions are reportedly produced by any strong deoxidizer such as aluminum, titanium or zirconium. Sims[6] argues that this is not an alloying effect, but rather it stems from deoxidation which appears to:

1. Increase the solubility of the sulphur in the steel so that the last metal to freeze is sulphur rich and solidifies as a eutectic.
2. Lower the interfacial tension of the dendritic concentrate so it will spread along the grain boundaries. There is some support for this argument because Smith[8] has shown that if a liquid phase among the grains of a solidifying metal has a low interfacial tension and hence a nearly zero dihedral angle it will spread infinitely along grain boundaries.

When excess aluminum is added to the steel so that the residual aluminum content exceeds 0.01 per cent, formation of the type II sulphides gradually gives way to formation of the type III sulphide according to Sims[6,7]. This author suggests that the liquid sulphide breaks up into pools in the melt, indicating high interfacial tension and lower solubility than for type II inclusions. Since these inclusions are observed to have crystalline faces and reportedly are not part of a eutectic, they must have solidified before the steel. Again, these inclusions are located intergranularly but they leave most of the grain boundaries free of sulphide. Sims[6] does not show why the additional aluminum, normally expected to decrease the oxygen content even further, should start lowering the solubility. But he does point out that aluminum, silicon and carbon will increase the activity of sulphur in an iron melt and hence lower its solubility. In this type of inclusion, he argues that oxides would be almost eliminated and the iron sulphide content may be lower.

2. Phase Diagrams in the Ternary System Fe-Mn-S *

The ternary system Fe-Mn-S proposed by Wentrup[9] is shown in Fig. 1 and 1a. A large miscibility gap begins in the Mn-MnS system, borders the Fe-Mn binary and the FeS-MnS quasi-binary and stops just short of touching the Fe-FeS system. This indicates that a small manganese addition to an iron-sulphur melt causes the melt to split into two phases, one sulphur rich, the other sulphur poor. Further manganese additions cause increased differences in sulphur content

* Weight per cent is used throughout this thesis.

between the two phases. No other information on the center of the ternary system at lower temperatures has been published. The most important part of this ternary system for sulphur control in commercial steelmaking and in this study lies approximately within the triangle bounded by Fe-FeS-MnS because these are the phases which appear to be involved in the approach to equilibrium. The high manganese corner of the ternary is of little concern in this study.

Consider the Fe-FeS system in Fig. 2 constructed by Chipman[10]. It can be seen that both Fe and FeS are completely miscible in the liquid phase but that cooling to 988°C produces a eutectic at 31 per cent sulphur. Thus in a typical iron-sulphur alloy containing 0.05 per cent sulphur or less as in many steels, the melt would be almost completely solidified before the eutectic composition is reached. The compound FeS is typically nonstoichiometric and should be written FeS_x, where x varies from 1.0 to 1.14[11].

The solid solubilities of sulphur in high purity iron have been determined by Rosenquist and Dunicz[12] as shown in Fig. 3. The maximum solubility of sulphur at 1,365°C was found to be 0.18 per cent in δFe and 0.06 per cent in γFe, while at 913°C, αFe was found to hold 0.02 per cent. These data, although indicative of decreasing solubility with decreasing temperature, are of little value in studying the Fe-Mn-S ternary because manganese has long been known to appreciably decrease the sulphur solubility in steel at all temperatures to insignificant levels. Thus Sim's argument for type III inclusions that aluminum, silicon and carbon lower the solubility of sulphur in an iron melt could be a relatively small factor when manganese is present at steelmaking levels.

The quasi-binary FeS-MnS proposed by Wentrup[9] and shown in Fig. 1 is the only comprehensive diagram of this system published to date. The diagram shows a eutectic at 1,180°C and six per cent MnS with a maximum solubility limit of 75 per cent FeS in MnS. Data of Chao et al[13] corroborated these values placing the eutectic at 1,181 ± 6°C with the solubility limit at 72 per cent FeS. The NaCl type structure of the compound MnS is the only one found in steels, although other structures will crystallize if the correct aqueous solutions are used. MnS is apparently stoichiometric and recent work of Chao et al[14] has confirmed values of 36.8 ± 0.2 per cent sulphur in various single crystals. These authors also indicate the solid solubility limit of FeS in MnS is considerably higher than indicated by Wentrup.

CHAPTER III

Theory

The mechanism of sulphide formation and alteration during ingot solidification and soaking has received little theoretical consideration. The present knowledge of solidification and crystal growth phenomena in low melting point metals and alloys is a necessary background for understanding these events in iron-base alloys. The means now available for analysing diffusion structures in ternary systems should be powerful tools for studying the equilibrium of sulphides with iron.

1. Solidification of Metals and Alloys

Formation of a dendritic pattern upon solidification of a pure metal is evidence of thermal supercooling according to Winegard[15]. That is, at the liquid-solid interface the liquid has a negative temperature gradient as shown in Fig. 4. The more extensive the supercooling, the faster the rate of solidification. Nuclei that form on an initially planar interface extend into lower temperature regions and will grow at the expense of their less advanced neighbours. Thus non-planar interfaces will become the stable configuration for growth of the solid as long as the temperature gradient in the liquid is negative.

Supercooling is also required for alloy solidification in a dendritic pattern. But in the case of alloys, supercooling can be produced not only by negative temperature gradients in the liquid, but also by constitutional means accompanied by a positive temperature gradient. Rutter and Chalmers[16] developed the basic concept for the present understanding of constitutional supercooling and Tiller et al[17] presented the argument quantitatively.

Essentially the theory of constitutional supercooling holds that if a binary alloy of composition Co freezes to precipitate a solid with a lower concentration of solute, then the liquid adjacent to the solid will become richer in solute than Co. Fig. 5 shows the freezing of a simple binary alloy of composition Co where the distribution coefficient, Ko, is less than 1. Ko is defined as the ratio of the concentration of solute in the solid to the concentration of solute in liquid when both phases are in equilibrium. The higher solute concentration in the liquid will produce a higher solute concentration in the next liquid to freeze. Thus a steady-state will result when the solid rejects solute at the interface at a rate equal to the solute diffusion away from the interface into the liquid. Under steady-state conditions, a decreasing exponential solute distribution will be established in the liquid ahead of the solid-liquid interface, Fig. 6. Further, the liquid at every concentration in the solute distribution has an equilibrium freezing temperature determined by the phase diagram, Fig. 7. When the real temperature in the liquid is compared with equilibrium liquidus temperature it may be found that

there is a zone of supercooled liquid in front of the solid-liquid interface, Fig. 8. Such a condition is called constitutional supercooling and its extent depends directly on the concentration gradient in the liquid. Winegard[15] has discussed this subject in great detail with respect to low melting point alloys.

In an alloy ingot, three zones of grain structure are usually found after solidification, Fig. 9, and these can be related to supercooling. The narrow outside zone at the mould face contains equiaxed grains which result from thermal supercooling because of the rapid heat removal through the mould wall. The relatively wider intermediate columnar zone results from competitive growth of the most favourably oriented crystals of the chill zone in the slightly supercooled liquid. As solidification continues, supercooling intensifies and dendrites start to form. Depending on the separation of the solidus and liquidus, marked constitutional supercooling will occur and new crystals will nucleate heterogeneously to form the central zone of the ingot. Because the nuclei of the new crystals are unassociated with the existing columnar ones, the orientations of the new crystals are random.

Although these arguments have thus far been supported by experiments with low melting point binary alloys[15], the same three zones of crystal types are found in multicomponent iron-base alloys. Therefore, the supercooling and solidification concepts should be qualitatively applicable to higher melting point ternary alloys in the Fe-Mn-S system.

2. Coring, A Non-equilibrium Condition

The foregoing discussion has considered solidification of alloys under local equilibrium conditions at each temperature in the zone, but in practice equilibrium during cooling is rarely attained due to slow diffusion in the solid. This necessitates consideration of an additional phenomena called coring which introduces concentration gradients into the crystals.

Because mixing in the liquid by convection and diffusion is so much faster than diffusion in the solid state, the solid is usually unable to alter its composition throughout to follow the equilibrium solidus curve indicated by the phase diagram[18]. This results in coring where the centre of the resulting crystal is richer in the higher melting point constituent than the average for the whole alloy, and where the last metal to freeze is much poorer in this constituent. For example, in Fig. 10, the first material to solidify at temperature T_1 has the composition a on the equilibrium solidus curve abc. However, because solid state diffusion is so slow, this material does not achieve saturation as the temperature falls and its solubility for the lower melting point component increases. In the extreme case where solid state diffusion is negligible, the centre of each crystal would remain at the composition a which froze initially. At any given temperature then, only the outer layer of each crystal or dendrite has the composition indicated by the equilibrium solidus abc and the average composition is somewhat less in the low melting point component as shown by curve ab'c'. When the temperature falls to that of the equilibrium

solidus for the overall alloy given by T_2, the average composition of the solid b' will be depleted of the lower melting point solute which is still retained in the melt. With continued cooling, the remaining melt will change in composition approximately according to the equilibrium liquidus line def (or its projection if a eutectic can be formed) while the outer layers of solid will continue to accumulate on the crystal in accordance with the solidus curve abc until the average composition of the solid equals the overall composition of the alloy at T_3. At this temperature the remaining liquid, rich in solute, will freeze and further enhance the compositional differences between the core and surface of the crystals.

The phenomenon of coring is responsible for the dendritic segregation of manganese in iron which has been shown to be large compared to that for other common alloying elements in steel[2]. It should be noted too that the sulphide phase which has very limited solubility in solid iron[12] will be pushed ahead of the solidifying interface and finally solidify interdendritically to remain in intimate contact with high manganese concentrations.

3. Diffusion in Ternary Systems

In a ternary system, the second independent concentration variable introduces an extra degree of freedom not found in binary alloys. This may cause the planar interface of a ternary diffusion couple to become unstable and thereby produce interface configurations which are difficult to interpret in terms of diffusion. Two

general approaches to studying ternary diffusion phenomena have met with some measure of success. The first approach takes the phenomenalogical equations and after choosing suitable values for diffusion coefficients predicts a virtual path for diffusion on a ternary isotherm. Such a path may or may not be confirmed by experimental diffusion couples, depending on the phases between the terminal compositions on the isotherm. The second method has concerned itself with morphological change during oxidation or liquid metal attack of binary alloys, one component of which behaves in a noble manner. Although both approaches contribute much to an understanding of ternary diffusion, it appears that considerably more work is required before their equivalence will be demonstrated.

(i) Phenomenalogical Equations and Diffusion Paths

The basis of the phenomenalogical equations for diffusion starts with Fick's first law[19], which relates the diffusive flow or flux J, and the concentration gradient ∇C by

$$J = -D\nabla C \qquad (1)$$

where D by definition is the diffusion coefficient. When this relationship is combined with the mass balance

$$\text{div } J + \frac{\partial C}{\partial t} = 0 \qquad (2)$$

Fick's second law results

$$\frac{\partial C}{\partial t} = \nabla . \left[D(c) \nabla C \right] \quad . \qquad (3)$$

For a ternary system with two independent components having concentrations C_1 and C_2 which diffuse in one direction in a single phase, it is possible to rewrite (3) so that

$$\frac{\partial C_1}{\partial t} = \frac{\partial}{\partial x}\left(D_{11}\frac{\partial C_1}{\partial x}\right) + \frac{\partial}{\partial x}\left(D_{12}\frac{\partial C_2}{\partial x}\right) \qquad (4)$$

and

$$\frac{\partial C_2}{\partial t} = \frac{\partial}{\partial x}\left(D_{12}\frac{\partial C_1}{\partial x}\right) + \frac{\partial}{\partial x}\left(D_{22}\frac{\partial C_2}{\partial x}\right) \qquad (5)$$

where the D's are functions of C_1 and C_2. For these equations, parametric solutions have been sought which give rise to two ordinary non-linear differential equations[20,21,22].

In the initially-stepped infinite diffusion couple produced by holding the terminal compositions in intimate contact, the behaviour of diffusing atoms can be very complex because the extra degree of freedom in ternary systems may allow supersaturation in some regions leading to precipitates or non-planar interfaces[23,24,25,26]. Kirkaldy and Brown[23] have stated that if all interfaces of the intermediate phases are planar then it frequently may be possible to obtain parabolic solutions at phase interfaces with due regard for the parabolically expressed interface continuity relations[27]. Such a solution endorses the idea of infinitesimal equilibria which presumes that concentrations at adjacent interfaces of infinitesimally thin layers of the structure are in equilibrium. A calculated diffusion path through unsaturated regions should describe the physical sequence observed in a suitable diffusion couple. But if the calculated path enters supersaturated regions on the ternary isotherm, its trace is

terms of the same parameter, λ. However, the penetration curves cannot be derived from the diffusion path since most of the kinetic data are discarded in the isothermal plot.

Regardless of the type of interfaces in the couples, the diffusion path must cross the straight line joining the terminal compositions at least once since, as stated previously, the mean composition of the couple must lie along this straight line.

Diffusion paths in two-phase regions suggest several phenomena depending on their course. Paths coinciding with tie lines specify that the two phases connected by the tie line are in equilibrium across a planar interface. By convention, this portion of the path should be dashed to indicate that it represents no spatial extent in the couple. When paths enter a two-phase region from one phase and return to that same phase after crossing tie lines, they delineate a region of isolated precipitates. Diffusion paths leaving one-phase zones, cutting tie lines and continuing on in other phases characterize non-planar interfaces which may appear as columnar-plus-isolated precipitate or purely columnar regions in the couple. In the two-phase areas, diffusion paths do not reverse the order of cutting tie lines because the components' activities are single-valued functions of position on the phase boundary.

Diffusion paths in three-phase regions may be approximated by straight lines whose termini represent the local equilibrium existing at a planar multiphase interface. Again, because such paths represent infinite proximity in the couple they should be portrayed as dashed lines on the ternary isotherm. Finally, paths must leave the triangles

on sides opposite to those which they entered otherwise there would not be single values for the activities of components at the tie-line terminals.

(ii) Attack of Binary Alloy Surfaces by Liquid Metal

The second approach to diffusion in ternary alloys is concerned with the attack of binary alloys by oxygen or by liquid metals. Wagner[25] has shown for binary alloys involving a noble metal that an oxide film is stable with uniform thickness if diffusion in the alloy is fast with respect to diffusion in the oxide but that it is unstable when diffusion in the alloy is slower. When solid alloys are in contact with a liquid phase, one of the components is likely to be more soluble than the others and hence the liquid phase may penetrate the solid irregularly.

Harrison and Wagner's study[28] on the effect of liquid silver in contact with solid copper nickel alloys appears relevant to the case of liquid FeS interacting with solid iron-manganese alloy. At high temperatures, the copper was highly soluble in the liquid silver but the nickel had limited solubility. By introducing calculations parallel to those for oxidation of binary alloys containing a noble metal[25], the authors showed that a plane solid-liquid interface could not remain stable. Starting with a slight perturbation of the plane interface on the atomic scale, it was argued that the effective length for copper diffusion was less at some points than at others. Thus more copper was lost to the liquid from that part of the perturbation requiring the shortest diffusion distance and the amplitude of the perturbation increased with time producing a macroscopic non-planar interface.

Two limiting cases for the silver liquid penetration of the copper-nickel alloy were anticipated by Harrison and Wagner. The first case visualized widely spaced fingers of liquid silver entering the alloy and leaving broad projections of alloy with essentially the original composition. In the second instance, numerous closely spaced liquid penetrations were separated only by narrow columns of the less soluble nickel.

In the apparently analogous case of liquid FeS in contact with solid iron containing a low percentage of manganese along an initially planar interface, it is expected that the liquid FeS should penetrate the alloy. This case is related to that of copper-nickel-silver because the liquid FeS will not dissolve the second component, iron from the alloy. Hence only manganese dissolves and at a rate proportional to diffusion in the solid alloy. Based on Harrison and Wagner's argument[28] for the general case of a solid alloy A-B under attack by a liquid C in which only A is soluble, the rate of recession of the solid-liquid interface with respect to liquid FeS in contact with solid Fe-Mn will be considered.

For an initially plane solid-liquid interface, the mole fraction of iron, N_{Fe}, in the Fe-Mn alloy is a function of distance, X, from this interface and of time, t. Hence for the rate of change of concentration

$$\frac{\partial N_{Fe}}{\partial t} = D \frac{\partial^2 N_{Fe}}{\partial x^2} \qquad \text{for } X > X_t \qquad (6)$$

where X_t designates the interface motion after time t, and the diffusion coefficient, D, in the alloy is considered independent of concentration.

Since the manganese is highly soluble in liquid FeS and its concentration in the solid Fe-Mn is low, the solid alloy at the interface will be essentially pure iron after time t. That is

$$N_{Fe} \simeq 1 \quad \text{at} \quad X = X_t \qquad . \qquad (7)$$

Because iron does not enter the liquid FeS, it must diffuse backward from the advancing interface at a rate equal to that of the penetrating liquid, μ, where

$$\mu = dX_t/dt \qquad . \qquad (8)$$

Combining Fick's first law and the mass balance yields

$$N_{Fe}\,\mu = D\,\frac{\partial N_{Fe}}{\partial x} \quad \text{at} \quad X = X_t \qquad . \qquad (9)$$

A further initial condition is that

$$N_{Fe} = N'_{Fo} \quad \text{at} \quad X > 0,\ t = 0 \qquad (10)$$

where N'_{Fe} is the initial mole fraction of iron in the solid. Assuming the alloy sample is sufficiently large to apply the solutions for a stepped infinite couple, Wagner and Harrison[28] argue that the above equations are satisfied by a solution of the form

$$N_{Fe} = N'_{Fe} + (1 - N'_{Fe})\,\frac{\text{erf}\,(X/2Dt)^{1/2}}{\text{erf}\,\alpha} \qquad (11)$$

and

$$X_t = 2\alpha(Dt)^{1/2} \qquad (12)$$

where the dimensionless parameter α is given by

$$\alpha \simeq N'_{Mn}/\pi^{1/2} \quad \text{for } N'_{Mn} \ll 1 \qquad . \qquad (13)$$

Combining (12) and (13) gives for plane interfacial movement

$$X_t = 2N'_{Mn}(Dt/\pi)^{1/2} \quad \text{for } N'_{Mn} \ll 1 \qquad (14)$$

This plane interface is not stable according to Wagner's theory[25] and experiments[28] and hence the rate of attack of deeply penetrating wedges of liquid must be considered. In the first limiting case mentioned previously where the fingers of liquid are widely spaced, the diffusion of manganese into the liquid parallel to the initial surface corresponds to diffusion from an infinite space. The penetration depth, X_p, of a single finger of liquid FeS perpendicular to the original interface has been shown[28] for the general case to be of the form

$$X_p = (3\ K\ N'_{Mn}\ D'_{Mn}\ t)^{1/2} \quad \text{for} \quad N'_{Mn} \ll 1 \qquad (15)$$

where K is the distribution coefficient for the soluble metal between liquid and solid, D'_{Mn} is the diffusion coefficient of the soluble component in the liquid phase and N'_{Mn} is the mole fraction of the soluble component in the liquid in equilibrium with solid of the initial composition.

In the second case where the liquid wedges are closer together, the penetration depth for the general case was given[28] in the form

$$X_p = 2(K\ N'_{Mn}\ D'_{Mn}\ t)^{1/2} \quad \text{for} \quad N'_{Mn} \ll 1 \qquad (16)$$

Although the physical conditions underlying (15) and (16) are essentially different, they yield similar values of X_p, according to Harrison and Wagner[28], which are much larger than the value of X_t for planar interface movement.

As pointed out by Harrison and Wagner[28], the main assumptions in calculating the expressions for X_p are noteworthy since they may not be strictly applicable. First, liquid and solid at the tip of a wedge may not be in equilibrium and the geometry of the finger near the tip could be influenced by local dissolution and redeposition of iron as well as dissolution of manganese. Further, side branching of penetrating liquid was not considered but these authors have found this effect experimentally. This configuration would tend to decrease the depth of penetration. Finally, the liquid does not always penetrate perpendicular to the original interface and this also reduces the expected penetration distance. Hence Harrison and Wagner only consider the values of X_p in (15) and (16) as upper limiting values rather than definite values and this has been born out in their experiments with the copper-nickel-silver couple[28].

CHAPTER IV

Electron Probe Microanalysis

The electron probe used for microanalysis is essentially an instrument with magnetic lenses designed to focus an electron beam at a cross-over point of roughly 1μ diameter where it enters the solid surface of a specimen whose chemical composition is to be determined. Selection of a specific area of the specimen is aided by an optical viewing system. The 1μ diameter electron beam irradiates about $1\mu^3$ causing it to emit a complex X-ray spectrum including the characteristic radiations of the contained elements. Analysis of the X-rays by means of a spectrometer and a detector provides both qualitative and quantitative data about the elements in the selected volume.

Many metallographic features such as inclusions, precipitates and penetration zones in diffusion couples which frequently require quantitative analysis are amenable to study by the electron probe. Analysis of these features requires standards of known composition in order to correlate sample composition with intensity. In addition, for ternary and higher order systems where standards of uniform composition are not readily obtained, it is useful to determine absorption, fluorescence and atomic number corrections for the observed intensity. These corrections will be discussed later.

1. Excitation of X-rays in the Electron Probe[29,30,31]

X-rays are excited when a potential difference, usually in the order of 25 to 35 K.V., draws electrons from the filament through the magnetic lenses to the sample. The X-rays, which radiate in all directions from the point of electron impingement, are produced by less than one per cent of the kinetic energy of the electrons. Most of the kinetic energy changes to heat. X-rays consist of a mixture of wavelengths and the variation of intensity with wavelength depends on the applied voltage. Intensity is defined as the rate of flow of energy through unit area perpendicular to the wave motion. Fig. 12 shows a schematic plot of X-ray intensity vs. wavelength for one element at one typical operating voltage. The intensity is zero up to a certain wavelength called the short wavelength limit, λ_{SWL}. With increasing wavelength, the intensity rises rapidly along a smooth curve called continuous or white radiation. Providing the voltage is above a certain minimum value, as required in the electron probe, peaks such as K_α and K_β interrupt the smooth curve. Wavelengths of these intensity maxima are characteristic of the particular element excited and hence are called characteristic X-rays.

The continuous spectrum arises when electrons hit the target because of the fact that electrically charged particles emit energy when decelerated rapidly. However, not all electrons lose energy in the same manner. Some are stopped in one impact with an atom giving rise to X-ray quanta of maximum energy and minimum wavelength. Other electrons lose fractions of their energy after each of several impacts

thus emitting smaller amounts of energy with longer wavelengths. The whole spectrum of wavelengths represented by the smooth curve from λ_{SWL} upwards constitutes continuous radiation. It can be anticipated that a slightly higher accelerating voltage for electrons will shift the continuous spectrum to the left since the number and average energy of the quanta are increased. In probe analysis it is desirable to minimize the continuous spectrum because it gives no information about the particular elements of interest.

2. Analysis of the Spectra[29,30,31]

The characteristic X-ray spectra emitted by the small volume element in the sample must be analysed for wavelength and intensity before the chemical composition can be determined. There are two principal ways to isolate characteristic X-rays from the various specimen elements. The first method, called crystal diffraction, produces X-rays of one chosen wavelength because only one wavelength is diffracted for each incident angle setting of the crystal, according to the Bragg Law. The second method, energy dispersion, uses an electronic filter in a detector circuit to pass only a particular X-ray energy corresponding to a selected characteristic wavelength. Energy dispersion is not as efficient in separating characteristic X-rays as is crystal diffraction, particularly at low chemical concentrations. Hence, in probe analysis, the drawbacks to energy dispersion are overcome when detectors are used simultaneously with spectrometers (Fig. 13). The spectrometer, when set to diffract only one desired wavelength, will pass on to the detector only quanta of one energy level. This

combination greatly reduces the background relative to the characteristic radiation of interest and hence improves the sensitivity of the electron probe microanalysis.

3. Intensity vs. Chemical Composition

To a first approximation, when a high energy electron strikes either an element in an alloy or a pure element, the number of ionizations in the detection counter is proportional to the intensity of the incident X-rays. Hence for electron probe microanalysis, Castaing[32] derived a relation of the following form:

$$\frac{n_A}{n_{100A}} = \frac{I_A}{I_{100A}} = W_A \qquad (17)$$

Here, n_A and n_{100A} are the number of ionizations from the alloy and pure element respectively, I_A and I_{100A} are the intensities from the alloy and pure element and W_A is the mass concentration of the element in the alloy. This relationship holds strictly for X-rays produced in atoms of the sample before absorption and other matrix effects exert their influence. The simplicity of the relationship arises because the radiations being compared are identical in all aspects except those arising from travel in the sample. Thus factors such as absorption in passing through windows between the sample and the ionizing chamber and spectrometer inefficiency are cancelled because they occur in both terms of the ratio. The quotient of the two intensities after correction for matrix absorption, atomic number differences and fluorescence gives, for most practical purposes, an accurate ratio of the element in the alloy to the element in the pure state regardless of configurations

in the particular probe design such as the angle of electron incidence and the angle of X-ray take-off.

(i) Matrix Absorption for Characteristic X-rays

Characteristic radiation of an element is usually absorbed differently by other elements than it is by the radiating element itself. Thus, if an element is in an alloy whose other components have relatively higher or lower mass absorption coefficients, then its apparent radiation will be relatively reduced or increased in intensity respectively as it emerges from the specimen.

These effects have been investigated by several researchers, including Castaing[33,34] and Castaing and Descamps[35]. Castaing introduced a parameter X defined as

$$X = \mu' \csc \phi \qquad (18)$$

where μ' is the mass absorption coefficient and ϕ is the angle between the sample and the X-rays entering the spectrometer. The absorption correction which depends on both the accelerating voltage and on the atomic number of the specimen is calculated by means of f(X) functions. Unfortunately, these conditions stipulate that a double family of curves is required to calculate absorption corrections and only a limited number of f(X) curves is presently available. Philibert[36] also has contributed to absorption corrections by deriving an analytical expression for the f(X) function.

Birks[31] has developed a relatively simple method for correcting intensity ratios for matrix absorption. His calculations result in a modified version of equation (17):

$$\frac{I_A}{I_{100A}} = W_A \frac{F_A}{F_{100A}} \qquad (19)$$

where F_A and F_{100A} are intensity functions for element A in the alloy and in the pure state. Both of these functions depend on the total absorption coefficient for A radiation, the take-off angle and the accelerating voltage.

(ii) Atomic Number Effects on Electron Excitation

The electron excitation at a given distance X beneath the surface of the specimen depends on the number of electrons stopped in a specimen of density ρ at that depth. In calculating the production of X-ray quanta the mass per unit area, ρx, of material traversed by the electrons is usually considered[31, 33, 36]. The stopping power coefficient decreases for increasing atomic numbers and it is assumed that the stopping power of an alloy is a linear combination of the stopping powers of its constituent elements. If this were the only factor at work, the true relation between the concentrations and the characteristic emissions would depart considerably from linearity except in the case of alloys containing elements close together in atomic number.

Luckily, this stopping power effect can be offset by a difference in electron backscattering between the alloy and the pure element. Backscattering is the loss of electrons from the specimen while they still retain sufficient energy to produce X-rays and it results in the production of less quanta. At moderate accelerating voltages of approximately three times the excitation potential, this backscattering effect which increases with increasing atomic number is compensated for by the decrease in stopping power. Birks[31] has developed an easily applied method to

account for atomic number differences by deriving simple multipliers for the total mass absorption coefficients depending on the accelerating voltages.

(iii) Matrix Enhancement for Characteristic X-rays

Corrections for matrix enhancement are concerned with the additional characteristic radiation excited in element A by fluorescence from element B. Several researchers including Castaing[33] and Wittry[37] have attempted to evaluate fluorescent enhancement from fundamental parameters, but the calculations are long and involved. Birks[31] has developed an approximate empirical expression for enhancement in terms of three parameters:

1. the intensity of characteristic B radiation excited at a given depth in the specimen.
2. the fraction of characteristic B radiation absorbed by element A.
3. the excitation efficiency for B radiation in producing A radiation.

The resulting expression is readily determined and is equivalent to multiplying the R.H.S. of equation (19) by $(1 + K_F)$ where K_F is called the total enhancement coefficient. The relationship between intensity and mass fraction can now be written as follows:

$$\frac{I_A}{I_{100A}} = W_A \frac{F_A}{F_{100A}} (1 + K_F) \qquad (20)$$

Birks[31] claims that when atomic number multipliers are used, this equation will give intensities correct to within ± 2 per cent of the amount present in the alloy. Thus, for most electron probe microanalyses this equation used in conjunction with suitable standards should give reasonable values of mass fractions in alloys. More accurate analyses are likely to be obtained only by exclusive use of standards at the present time.

CHAPTER V

Experimental Methods

The equilibrium between iron and iron-manganese sulphides was studied by two types of experiments. For temperatures near the solidification point of iron, two to three grams of iron were equilibrated with the sulphide phases in the electromagnetic levitation coil and then quenched in mercury. The second type of experiment was designed to investigate the equilibrium at 1300°C, a temperature representative of ingot soaking. Finite diffusion couples comprising liquid FeS in a solid Fe - 3.16 per cent Mn container were equilibrated in a high frequency heating coil and then quenched in a stream of hydrogen. In a modification of this technique, both FeS and Mn were enclosed in high purity iron containers and equilibrated. Specimens from all experiments were examined metallographically and representative samples were analysed by electron probe techniques.

1. Materials and Specimen Preparation

The following materials were utilized in preparing specimens for levitation and diffusion experiments:

	C	Mn	P	S	Si	Cu	Cr
Westinghouse "Pure Iron" Spectrographic Electrodes	0.001%	not detected	0.001%	0.004%	--	--	--
	(guaranteed to contain at least 99.95% Fe)						
Electrolytic Fe-Mn Alloy	0.05%	3.16%	0.011%	0.014%	0.035%	0.001%	0.018%
Iron Wire 0.009" dia.	0.06%	0.08%	0.009%	0.008%	0.003%	--	--
Battelle, High Purity Iron	Impurities 25 ppm. metallic, 11 ppm. nonmetallic						
Electrolytic Manganese	--	99.5%	--	--	--	--	--
Ferrous Sulphide	Commercial Purity						

For the last two Battelle iron containers, iron sulphide was prepared by levitating Battelle iron in a hydrogen atmosphere and dropping it into a graphite crucible full of sulphur, where the exothermic reaction yielded a high purity product.

Specimens for levitation were prepared by cutting a 5/8 inch length from the electrodes and drilling a 1/4 inch hole axially to a depth of 5/16 inch. Then a 1/16 inch thick disc was machined from the electrodes to fit snugly in the hole and a loop of the 0.009 inch wire was tied around it diametrically. After the manganese and ferrous sulphide additions were weighed and placed in the cavity, the disc and wire assembly was forced into the hole ready for levitation (Fig. 14(a)).

The diffusion couples were prepared by drilling 7/64 inch holes into small pieces of the Fe - 3.16% Mn alloy. A weighed amount of ferrous

sulphide was placed in the drill hole and the opening was plugged by a short length of "Pure Iron", machined to fit tightly (Fig. 14(b)). In the modified technique, containers were made from the "Pure Iron" electrodes and from the Battelle high purity iron. Both ferrous sulphide and manganese were added to these pots. The last two pots had iron sulphide made by levitation melting. Openings in the pots were plugged with material identical to that of the containers and the final pot had the top sealed by argon arc welding.

When the specimens were quenched in their respective experiments, they were sectioned with a jeweller's saw, mounted in lucite and metallographically polished. The final surface was prepared by polishing on Buehler microcloth impregnated with 1 micron diamond grit and lubricated with kerosene. After examination by optical microscope, the samples were placed in an evaporator and coated with carbon a few angstroms thick to provide electrical conductivity in the electron probe.

2. Levitation Apparatus and Procedure

The levitation apparatus, Fig. 15, was supported on a trolley and consisted essentially of a 15 mm. glass tube, about which 1/8 inch copper tubing was coiled and connected to a 10 KVA, 450 KC/S Tocco generator. The coil configuration was similar to that described by many researchers, including Polonis, Butters and Parr[38], Harris and Jenkins[39] and Jenkins, Harris and Baker[40]. The bottom of the coil consisted of five turns around a former comprising a 15 mm. spigot, which tapered into a 60° angle cone. The bottom two turns were wound coplanar on the spigot

and the upper three turns were wound helically on the cone. After removing the coil former and inserting 15 mm. O.D. glass tubing expanded to conform to the coil configuration, two reverse turns were wound helically around the glass about 1/4 inch above the lower part of the coil. This configuration provided adequate lift and lateral stability for levitating specimens. The top of the glass tubing was connected by plastic tubing to a glass top with three tubes designed to exhaust gas, admit specimens and permit viewing through an optically ground pyrex flat. This arrangement is shown in Fig. 16. The bottom of the coil-wound tube was inserted in an iron-sleeved brass block containing mercury and fitted with a gas inlet tube.

Auxiliary apparatus required for successful levitation included tanks of He and H_2 for preventing oxidation and controlling temperature. A two-colour optical pyrometer sighting through a 45-90 prism on the optical flat indicated specimen temperatures to within ±10°C. The levitation coil was cooled by water flowing from a source separate from the generator and by air directed from above. Supercooling of the specimen was virtually eliminated by touching the levitating sample with the tip of 0.009 inch wire suspended from a small piece of soft iron, manipulated from outside the glass tubing by a horseshoe magnet.

To begin a run in the levitation unit, the system was first flushed with He. Then the specimen was suspended on an iron wire hook, lowered into the coil, and heated rapidly above the Curie Point, 768°C, where it levitated and melted. Then the wire nucleator was dropped down the tube and caught by the magnet, suspending it above the specimen. Thereafter,

the sample entrance was sealed with a rubber stopper, H_2 was introduced and the He flow was stopped. After equilibrating the two phases of the melt for about a minute at the solidification temperature of iron, the H_2 flow was increased slightly and the iron nucleator was touched to the specimen, causing the iron to solidify from the top to the bottom. After equilibrium was established for one or two minutes, the power was cut and the magnet was pulled away, allowing the specimen to precede the nucleator into the mercury quench.

3. High Frequency Heating Apparatus and Procedure

The Fe - 3.16% Mn couples and the high purity Fe containers were equilibrated with their contents in a high frequency heating apparatus fastened to a trolley (Fig. 17). Primary features of the unit were a 1/4 inch diameter copper tube with six helical turns around a three inch diameter vycor tube, three feet long (Fig. 18). The above-mentioned Tocco generator supplied power and cooling water for the coil. Samples were placed on a thin disc of "Pure Iron" in the bottom of an alumina crucible balanced on the end of an assembly of refractories and a 1/2 inch diameter iron tube. The iron tube could be lowered to position the couple in the center of the coil for heating and raised to locate the specimen between two vertical copper tubes which exhausted H_2 at the crucible. The iron tube was perforated at the top and served as a gas outlet. Gas purity was improved by forcing it through platinum gauze and magnesium perchlorate to remove water and through ascarite to absorb CO_2. Temperatures were measured as for levitation with a two-colour optical pyrometer.

A run was initiated by positioning the couple or iron container in the crucible between the coil and flushing the pyrex tube with He or H_2. When the power was applied, the temperature was increased rapidly to 1300°C as indicated by the optical pyrometer and maintained by adjusting the power settings, rather than by controlling the gas flow rate. At the end of a run, H_2 was admitted through the two copper tubes, the power was cut off and the sample was thrust up between the two streams of exhausting H_2 to quench.

4. The Electron Probes

Three electron probes were used throughout the course of this study. The Philips probe at the University of Toronto and the Fisher Scientific probe in Boston were used to confirm the preliminary results obtained on the McMaster probe. This latter probe was built under the direction of Dr. G. R. Purdy and utilized the circuitry, electron gun, alignment coils and condenser lens of a Philips E.M. 100 electron microscope. To these components were added an objective lens, a light optical system and two flexing mica-crystal spectrometers. One spectrometer had a vacuum path and the other a continuously flushed He path. From each spectrometer a Siemens flow proportional counter and preamplifier fed pulses to a Philips rack of counting electronics, including a one channel pulse height analyser, an electronic counter and a rate meter. Appendix I gives an example of the procedure used to obtain settings yielding the highest peak to background ratio of counts for the elements using this equipment.

5. Calibration Curves for Microanalysis

Calibration curves giving the raw intensity from the electronic counter as a function of weight per cent in the ternary alloy were sought initially using standards alone. Attempts to produce homogeneous standards of ternary compositions by sintering, high frequency heating and levitation melting techniques met with limited success because the segregation was too extensive for standards on a micro scale. However, the elemental iron and manganese standards were readily available and an exceptionally homogeneous single crystal of MnS was obtained from Professor L. H. Van Vlack of the University of Michigan. Samples of FeS with acceptable levels of segregation were available commercially. Thus the use of these standards in combination with the theoretical calculations of Birks[34] appeared to be the most promising means of obtaining calibration curves for microanalysis of this system. Appendix II gives a sample calculation of intensities for one ternary composition. Typical calibration curves for iron and manganese in the ternary system are shown in Figs. 20 and 21, for the McMaster probe operating at 30 K.V.

CHAPTER VI

Results

The object of this investigation was to examine by metallography and electron probe microanalysis the phases liquid FeS, solid βMnS and solid Fe which exist in the portion of the Fe-Mn-S constitution diagram relevant to steel solidification. Equilibrium conditions were investigated at 1535°C by levitation melting and at 1300°C by iron pots containing Mn and FeS additions. Diffusion couples between liquid FeS and solid Fe - 3.16% Mn were designed to simulate Mn diffusion into the FeS at 1300°C.

1. Levitation Melting

The initial intent of the levitation technique was to trap sulphide inclusions in the levitated iron, to examine them metallographically and to probe representative sulphides in situ and thus determine their compositions. However, production of inclusions larger than four or five microns in diameter was difficult. Also, in many of the larger inclusions, tiny iron precipitates and fingers of iron extending into the sulphide phase were observed (Fig. 22). This iron phase in the sulphide prevented accurate microanalysis of the sulphide phase with three or four micron diameter electron beams.

Subsequently larger amounts of FeS were added to the iron until sulphide films six microns thick or more formed on the bottom surface of levitating specimens. These films were retained after quenching and cross-sectioning (Fig. 23). Micro-examination of the sulphide films showed that without exception, they contained iron precipitates and that the sulphide-iron interfaces were non-planar (Fig. 24).

The presence of αFeS, βMnS or both in the sulphide inclusions depended on the Mn/S ratio. Considerable sulphur was lost during levitation, thus an estimate of the final Mn/S ratio was difficult to make. However, initial Mn/S ratios less than about one produced mostly αFeS in the sulphide inclusions while initial ratios over 1.5 yielded only βMnS sulphides. Intermediate ratios gave mixtures of the two sulphides (Fig. 25).

In contrast to the inclusions, the sulphide films on the levitated specimens were always entirely βMnS. Regardless of how much the Mn/S ratio was lowered, no αFeS was observed in the sulphide films, even though inclusions in the iron adjacent to the interface were almost entirely αFeS. This is shown in a typical strip chart recording of X-ray line scans for Fe and Mn across a sulphide film-iron interface (Fig. 26). Scans giving images of absorbed electrons, backscattered electrons, Fe X-rays and Mn X-rays at the same location as the line scan are shown in Fig. 27.

2. Iron Pots Containing Mn and FeS Additions

The equilibrium between liquid FeS, solid βMnS and solid iron at 1300°C was investigated with the aid of iron pots. An iron plug retained most of the sulphide in the Pure Iron containers. However, when pots were made from the Battelle iron, most of the sulphide escaped past the plug. This was remedied by introducing a deeper pot with a plug approximately 1/4 inch long. Finally, when FeS prepared by levitation was added to the Battelle iron containers, it could be retained only after fusing the top of the assembly with an argon arc welder.

Micro-examination of the iron pots after heating at 1300°C for 30 minutes disclosed that the sulphide existed as almost entirely αFeS, a mixture of FeS and βMnS, or pure MnS depending on the ratio of Mn/S. Fig. 28a shows a photomicrograph taken with a blue filter, illustrating the light grey αFeS phase and the darker grey βMnS equilibrated with the Pure Iron container. Some very dark grey eutectic oxide also is present in the sulphide. The photomicrograph in Fig. 28b taken with partially polarized light at the same location shows that the boundaries between the sulphide phases are not clearly defined.

Examination of the high purity Battelle iron pots showed that the extent of each phase was several times larger than in the case of the lower purity systems. The two sulphide phases are shown through blue filtered light in Fig. 29a. Some very dark grey eutectic oxide is present within the αFeS. Again, as in the lower purity systems, the boundaries between the two sulphide phases are not sharply defined. The phases appear separated by a zone of phase mixture with an intermediate grey tone. This

is seen more clearly through polarized light, as in Fig. 29b. The phase mixture is much more discernable at high magnification (Fig. 30).

A typical strip chart recording of X-ray line scans for Fe and Mn in a Battelle iron pot (No. 8) is shown in Fig. 31. From right to left, the scan starts in βMnS, traverses a zone of phase mixtures, crosses a band of αFeS about 5μ wide and then enters a region of phase mixtures from which it never completely escapes. The whole scan was only about 10μ from an iron phase. Fig. 32 shows scanning images for absorbed electrons and X-rays from Fe, Mn and S in the line scan location. Similar scanning images are given in Fig. 33 for Battelle iron pot (No. 10) equilibrated with FeS and βMnS.

Tables I, II, IIa, IIb, IIc, IId, IIe and IIf give tabulations of data on the electron probes, the microanalysed pots and the point counts on the iron and the sulphide phases.

3. Diffusion Couples of Liquid FeS in Fe - 3.16% Mn Containers

In order to study the diffusion of Mn into the FeS phase at 1300°C, diffusion couples between FeS contained in an Fe - 3.16% Mn alloy were prepared. Very little difficulty was encountered in retaining the sulphide in the containers during heating (Fig. 34).

Micro-examination of cross-sections through the couples disclosed that the liquid sulphide penetrated the inside walls of the containers. In doing so the sulphide formed some βMnS and either left small iron precipitates or projections in the sulphide phase (Fig. 35), or it left large areas of iron behind the advancing sulphide interface (Fig. 36). At the sulphide penetration front, relatively fine globular precipitates formed

as shown in Figs. 35 and 36. Examination of these precipitates at high magnification through polarized light disclosed that they contained considerable amounts of a very dark phase and were generally darker than the adjacent βMnS phase as shown in Fig. 37. Many of the precipitates also had an iron phase in their core. Traces of the very dark phase, believed to be an oxide, were found associated with the sulphides throughout all of the diffusion couples.

Strip chart line scans for the X-ray intensity of manganese across the sulphide-iron interfaces invariably had the same profiles (Fig. 38). The 3.16% Mn in the Fe away from the sulphide fell off sharply to a low constant value at the fine precipitates and then increased abruptly on reaching the sulphide phases. Additional probing indicated that the manganese content of the iron phase everywhere behind the fine precipitates was approximately constant.

Table III lists the results of electron probe point counting on αFeS, βMnS and αFe phases in a representative diffusion couple.

CHAPTER VII

Discussion of Results

This discussion centers on the metallographic and microanalytic data from three types of experiments designed to survey equilibrium and kinetic conditions in the ternary system Fe-Mn-S. All three experiments comprising levitation melting, the iron pots and the diffusion couples offer both equilibrium and kinetic information. The following sections will emphasize the equilibrium aspects of the three experiments and the kinetic data will be incorporated in the final section.

1. Levitation Melting

The sulphide inclusions in the levitated specimens were too fine for reliable microanalysis with the electron probe. Therefore, we were able only to observe and record the coexistent phases at the solidification temperature of iron. These observations, along with other published results, suggest an isotherm of the construction shown in Fig. 39.

The isotherm illustrates the experimental observation that levitated specimens with Mn/S ratios in the order of 1.7 or greater always had βMnS inclusions throughout with no evidence of the αFeS phase. Lower ratios of Mn/S produced a combination of βMnS and αFeS in the inclusions (Fig. 25). The lower the ratio, the greater the amount of αFeS relative to βMnS. In principle, a knowledge of the Mn/S ratio at the first

appearance of αFeS in the βMnS and of βMnS in the αFeS should define two sides of the three phase region, γFe-liquid FeS-βMnS at 1300°C. However, a considerable amount of sulphur was lost during levitation and so the actual Mn/S ratios are uncertain.

The iron phase found within the small (generally less than 6μ diameter) inclusions of the levitated specimens (Fig. 22) presented problems in the microanalysis of the sulphides. The 2 to 4μ diameter electron beams of the McMaster and Toronto probes impinged on the iron phase in the sulphide and gave erroneous intensities for iron and manganese. However, the use of a probe such as the JXA-3A which has an electron beam diameter of 0.5μ may well make possible analysis of such inclusions.

2. Iron Pots Containing Mn and FeS Additions

The iron containers equilibrated with sulphide at 1300°C were the most reliable specimens for quantitative microanalysis. Results derived from the three electron probes, metallographic observations and published data are summarized in the ternary isotherm of Fig. 40.

Subject to the error arising from the fact that some of the sulphide escaped past the plugs of the iron containers during heating at 1300°C, the relative proportions of the αFeS and βMnS phases could be controlled by altering the Mn/S ratios. It was found that ratios in the order of one or more resulted in the formation of βMnS with no evidence of αFeS. Progressively lowering the ratios resulted in increasing amounts of αFeS relative to βMnS as in the case of the levitated specimens.

One of the most important observations in this experiment was the large dimensional increase in the sulphide phases after changing from

Pure Iron to the ultra high purity Battelle iron container (Figs. 28 and 29). This suggests that impurities such as oxygen play a prominent role in the growth of phases under equilibrium conditions. Indeed the difficulty of retaining the sulphide in the Battelle iron pots demonstrates that the interfacial tension of the sulphide was decreased when the oxygen content was lowered. This is in agreement with evidence from Smith[8] that a liquid metal with low interfacial tension will tend to spread along grain boundaries and with the observations of Sims[6] that sulphides which wet the grain boundaries are associated with lower oxygen in the iron than are globular sulphides.

Metallographic examination of the two sulphide phases in the Battelle iron pots suggests that they were equilibrated with iron at temperature. For example, two phases have assumed globular shapes wetted by the third (Fig. 30). Also, assuming the diffusion coefficient for Mn in γFe at 1300°C is in the order of 10^{-8} cm.^{2}/sec. and the time at temperature is 80 minutes (4800 seconds), then a rough calculation of the diffusion distance, S, can be made as follows:

$$S = (Dt)^{1/2} = (4800 \times 10^{-8})^{1/2} = 6.9 \times 10^{-3} \text{ cm.} = 69\mu.$$

Referring to Fig. 30, the large iron phase is measured as approximately 4 cm. across at 2250x or 18μ. Thus the diffusion distance for manganese is roughly four times the size of the iron phase and equilibrium should prevail at temperature.

The point counting data for the iron pots obtained from electron probes and recorded in Tables II to IIf permits only a semi-quantitative conclusion about the compositions of the three phase region FeS, MnS

and γFe at 1300°C. However, it can be seen from the microanalysis of pots Nos. 8 and 10, which, because of their high purity should yield the most accurate data, that the manganese content of the iron phase is very low, 0.03 per cent in No. 10 and not detected in No. 8. The sulphur concentration in the iron is below the limit of detectability. The tables also indicate that the sulphur concentration in both αFeS and β'MnS phases adjacent to the iron phase is on the average 9 or 10 per cent greater than expected if a pseudo-binary between stoichiometric FeS and MnS existed at 1300°C. The sulphur content in pots Nos. 8 and 10 decreases from a high of about 53 per cent in the αFeS to a low of roughly 45 per cent in the β'MnS. In the two phase regions of αFe-β'MnS the sulphur content approaches the value for stoichiometric β'MnS.

One interpretation of the high sulphur content in the FeS and β'MnS equilibrated with γFe is that the microanalysis is incorrect. However, considering that similar high sulphur readings were obtained with three different probes, this view appears unlikely. Furthermore, the magnitude of the observed difference is several times greater than the absorption corrections applied to the manganese and iron intensities from any of the three probes.

Acceptance of the probe results invites two explanations. First it is possible that the supposed pseudo-binary between FeS and MnS does not exist at liquid FeS temperatures and higher. However, a shift in phase boundaries at lower temperatures could bring about the appearance of a pseudo-binary or it could minimize the amount of the third phase present (γ or αFe) making it difficult to detect. Secondly, it is possible

that oxygen, which is known to be present to some extent in all specimens except pot No. 10, also could shift the equilibrium towards higher sulphur values. However, if oxygen content is a factor, then only a small amount of oxygen in the order of a few p.p.m. must be required for the equilibrium shift because every precaution was taken to eliminate oxygen from pot No. 10 and no oxides were observed metallographically.

3. Diffusion Couples of Liquid FeS in Fe-3.16% Mn Containers

The diffusion couple experiments qualitatively confirm the equilibrium data from the iron pots. Although the couples are essentially a kinetic experiment, it is reasonable to assume that local equilibrium exists in the couples. Indeed the manganese content in the iron was found to be low (roughly 0.20 per cent). Also, the sulphur contents of the αFeS and βMnS phases are higher than expected if a pseudo-binary exists (Table III). However, some discrepancy in sulphur values occurs and this is believed to result from the difficulty of positioning the electron beam in sulphide phases without striking iron precipitates or dendrites (Fig. 35). A higher value for iron intensity results in a lower value calculated for sulphur.

4. Kinetic Information

The ultimate aim of our study is to understand the history of formation of sulphides in commercial steels. This requires the equilibrium data as well as information about the transitional modes of the complex ternary system. A modicum of kinetic information may be inferred from our experiments, particularly the levitation and diffusion couple experiments.

The iron phases found within the inclusions of levitated specimens (Fig. 22), indicate compositional changes in the sulphide during or after solidification. Such changes appear to be in the direction of higher manganese concentrations in the sulphide. The shift to higher manganese requires the rejection of iron from the sulphide which could occur in the form of iron fingers or as a precipitate if a nucleation site, for example, a solid oxide, is present.

Sulphide films on the levitated specimens also presented some evidence for phase changes. The fact that no FeS could be formed in the sulphide films even though this phase existed as inclusions adjacent to the sulphide - iron interface suggests that the film was not completely equilibrated with the iron. This can be explained on the basis that the high frequency electromagnetic field in the iron provides almost all of the heat while the thin sulphide film is likely to be greatly cooled by the high velocity stream of hydrogen impinging on it. Thus it appears that βMnS is a more stable phase than liquid FeS at temperatures well below the solidification point of iron. This argument is further supported by the appearance of iron precipitates in the film and the fingers of iron extending into the sulphide layer (Fig. 24).

The band of phase mixture comprising αFeS and βMnS situated between the more extensive αFeS and βMnS regions in all of the iron pots (Figs. 29 and 30) is an undesirable artefact for equilibrium studies but it does contain some kinetic information. The band is believed to result from a shift of equilibrium during quenching. Evidence for this is the earlier argument that equilibrium did prevail and that oxides which are more soluble in the liquid FeS have outlined an apparent liquid FeS-βMnS

interface at 1300°C. Thus the existence of the band of phase mixture is interpreted as an attempt by the liquid FeS to penetrate the βMnS in search of manganese as the equilibrium shifted in favour of the βMnS formation at lower temperatures.

The diffusion couple experiments demonstrate that liquid FeS at 1300°C takes manganese from the Fe - 3.16% Mn container, rejects iron in the form of intrusions or dendrites and eventually forms a βMnS phase (Fig. 35). The observed amount of βMnS relative to αFeS depends on the amount of FeS originally present, on the sulphide diffusion time and on the rate of manganese diffusion in the sulphides and in the γFe at 1300°C.

Our observations on diffusion couples at temperature for various times up to 80 minutes suggest that two diffusion stages occur. In the initial stage during the first few minutes, iron dendrites penetrate the liquid FeS in response to the interfacial instability caused by manganese diffusion from the Fe-Mn phase (Fig. 35a). This interfacial instability and iron rejection from the sulphide is in agreement with the Harrison and Wagner argument[28] discussed earlier for the attack of binary alloys by a liquid metal. Further, following Kirkaldy et al[23] for diffusion in ternary systems, the path involving iron intrusions can be represented on a ternary isotherm (Fig. 40) by a solid line leaving the liquid FeS and crossing tie lines in the two phase liquid FeS-γFe region, and then by a dotted line parallel to a tie line joining with the γFe phase. It should be noted that the resulting S shape of the path is necessary for consistency with the mass balance. This follows from the requirement that the overall composition of any selected portion of the couple lie on a line joining

the termini. When the manganese from the alloy container has reached the far outside surface of the liquid FeS, a second stage of transformation can then begin. The excess manganese entering the liquid FeS is then able to initiate the formation of βMnS. That is to say, when manganese begins to pile up at the sulphide interface, the diffusion path must swing clockwise toward the three-phase region, thus instituting precipitation of βMnS. This can be seen in Fig. 35b, where the two sulphides αFeS and βMnS coexist with iron. At very long times, a finite system such as this will tend to attain some equilibrium distribution of βMnS and γFe.

It should be noted also that there is a tendency towards instability on the iron side of the original interface as well, due presumably, to diffusion of sulphur in this phase. This instability results in a layer of fine spherical sulphide precipitates (Fig. 35) which has characteristics of internal oxidation. This can be understood on the basis of ternary diffusion theory introduced in Chapter III, Section 3. However, since it appears here as an artefact, we will forego a detailed discussion.

In summary, the observed kinetic information tells us that manganese diffuses to the liquid FeS and βMnS phases as the temperature falls. However, no firm evidence has yet been found to indicate which initial sulphide phase is sufficient or necessary during cooling to instigate the observed sharp depletion of manganese in ferrite bands of commercial steel as indicated in the Introduction. The initial suggestion by Kirkaldy et al[1] that the manganese enrichment of βMnS depletes the surrounding γFe of manganese as the temperature falls has not been discounted. However, the strong tendency for manganese to diffuse to liquid FeS points the way to a model in which the above mechanism plays a secondary role. Clearly,

a knowledge of the non-equilibrium segregation paths on cooling liquid iron containing various Mn/S ratios appears necessary to pursue the problem further. Among other things, this will require the precise determination of one or more ternary isotherms between iron solidification and the ternary eutectic.

It is speculated that although the miscibility gap lies close to the iron corner of the diagram, the overall compositions of iron containing commercial amounts of manganese and sulphur may not lie in this region. Instead, it is thought that just below the solidification point of pure iron the overall composition enters a region of solid iron plus a liquid slightly enriched in sulphur. Further non-equilibrium cooling concentrates the manganese along the iron dendrites and pushes the sulphide to the intersection of some γFe grains. Thus the effective Mn/S ratio in the vicinity of liquid sulphide would be lower than the overall Mn/S ratio. In the presence of a nucleation center, say oxide, some of the sulphides could readily solidify depending on their composition, but other pockets of iron-rich sulphides may not be able to solidify until the ternary eutectic near the Fe-FeS system is reached. Also, the faster the cooling rate, the less time the iron-rich sulphide will have to adjust its composition. Thus the liquid sulphide requires more manganese to approach equilibrium but manganese can now only be obtained by diffusion through the adjacent solid iron. Hence the iron surrounding these sulphides would be sharply depleted of manganese as observed in the non-periodic ferrite bands of steel.

CHAPTER VIII

Summary of Results

1. Our knowledge of Fe-Mn-S isotherms at 1535°C and 1300°C has been extended. The present concention is given in Figs. 39 and 40.
2. As the Mn/S ratio in iron is changed the co-existing phases FeS or βMnS or both can be produced at equilibrium in the temperature range 1535°C to 1300°C.
3. Compositions lying in the three phase region at 1535°C will pass into the two phase region γFe-βMnS as the equilibrium temperature is lowered.
4. The concentration of manganese in γFe in equilibrium with liquid FeS and βMnS at 1300°C is at the limit of detectability with the electron probe.
5. Our observations suggest that the supposed FeS-MnS pseudo-binary does not exist at high temperatures. Indeed, we find that the three phase region liquid FeS-βMnS-γFe intrudes past the line joining stoichiometric FeS and MnS.
6. Liquid FeS has a high affinity for manganese when in contact with an Fe-Mn alloy at 1300°C and incites interfacial instability which assists its conversion to βMnS. Since similar iron intrusions appear in βMnS inclusions in commercial steels, there is a suggestion that these sulphides at some time during cooling may have been almost pure FeS.

CHAPTER IX

Recommendations

The following recommendations are proposed for the future pursuit of this study in the Fe-Mn-S ternary system:

1. Use iron pots with manganese and ferrous sulphide additions to study the ternary isotherms just below the solidification point of iron, say, 1520°C and just above the ternary eutectic, for example, 1000°C. The pot specimens have proven to be the most useful for obtaining quantitative equilibrium data at 1300°C with the electron probes and no difficulty is envisaged in extending the experiment to higher and lower temperatures.

2. Make diffusion pots only from ultra high purity iron, at least comparable to that supplied by Battelle and used in the final experiments of this study. The low impurity content is necessary to reduce the amount of oxygen in the system to a few p.p.m. or less.

3. Do not use commercial purity ferrous sulphide additions in the pots because of the relatively high oxygen content. Instead, prepare ferrous sulphide by the levitation technique mentioned in this thesis if non-stoichiometric compositions are acceptable. Otherwise, melt ultra high purity iron and sulphur in a carbon crucible and force hydrogen sulphide through the melt to approach the ferrous sulphide composition.

4. Use only high purity manganese additions which have been melted in carbon crucibles in a hydrogen atmosphere to remove oxygen.

5. Make the pots and the iron plugs sufficiently long that the tops can be sealed by argon arc welding without affecting the reaction zone. This will eliminate loss of sulphide during heating, at least at the lower temperatures and will minimize changes in the initial Mn/S ratiosof the additions.

6. Try small additions of iron oxide to pots with welded tops to assess more accurately the effect of oxygen on the phase diagram.

7. Increase the severity of the quench for the iron pots. This could be done by suspending the pots in the heating coil by a wire and then releasing the specimen, allowing it to fall into a mercury quench.

8. Consider the exclusive use of an electron probe with the smallest diameter electron beam spot, the clearest light optics and the highest peak to background ratio for counting. X-ray scanning facilities are highly desirable for any probe analysis in this system. One such probe suited to the study of this system is the JXA-3A. It has 0.5μ diameter focussed electron beam, polarizing light optics to facilitate distinction of αFeS and βMnS and a peak to background ratio of 2500 to 1 for accurate analyses. Large d-space crystals for analysing light elements such as oxygen also should be considered.

9. Try probe analysis of inclusions in levitated specimens with a 0.5μ diameter or smaller beam size.

10. Construct a model to determine the location of the eutectic troughs in the ternary system. Such a model, together with a knowledge

of the principles of solidification in ternary systems should facilitate the design of experiments to ascertain how sulphur-rich liquids will segregate with various cooling rates in systems having designated Mn/S ratios.

11. Construct a coil wound furnace suitable for heating the iron containers in hydrogen near the melting point of iron and incorporate facilities for controlling the cooling rate over a wide range of values and for interrupting the cooling at any time by quenching in mercury.

References

1. Kirkaldy, J. S., Brigham, R. J., Domian, H. A., and Ward, R. G., "A Study of Banding in Skelp", Can. Met. Quarterly, July-Sept. 1963, Vol. 2, No. 3, p. 235.

2. Kirkaldy, J. S., von Destinon-Forstman, J., and Brigham, R. J., "Simulation of Banding in Steels", Can. Met. Quarterly, July-Sept. 1962, Vol. 1, No. 1, p. 59.

3. Sims, C. E., "Electric Furnace Steelmaking", Chapter 21, 1963, Vol. 2, Iron and Steel Division, A.I.M.E., Interscience Publishers.

4. "Basic Open Hearth Steelmaking", Chapter 12, 1964, Physical Chemistry of Steelmaking Committee, A.I.M.E.

5. Metals Handbook, A.S.M., 1948, p. 445.

6. Sims, C. E., "The Nonmetallic Constituents of Steel", June 1959, Trans. A.I.M.E., Vol. 215, p. 367.

7. Sims, C. E., Saller, H. A., and Boulger, F. W., "Relative Deoxidizing Powers of Some Deoxidizers for Steel", Metals Trans., 1949, Vol. 185, p. 814.

8. Smith, C. S., "Microstructure", 1953, Trans. A.S.M., Vol. 45, p. 533.

9. Wentrup, H., Technische Mitteilung Krupp, 1937, Vol. 5, p. 131.

10. Chipman, J., "Iron-Sulphur", Metals Handbook, A.S.M., 1948, p. 1215.

11. "Physical Chemistry of Process Metallurgy", Part 2, 1961, p. 945, Metallurgical Society of A.I.M.E., Interscience Publishers.

12. Rosenquist, T. and Dunicz, L., "Solid Solubility of Sulphide in Iron", Trans. A.I.M.E., 1952, Vol. 194, p. 604.

13. Chao, H. C., Van Vlack, L. H., Oberin, F., and Thomassen, L., "Hardness of Inclusion Sulphides", Trans. A.I.M.E., 1964, Vol. 57, p. 835.

14. Chao, H. C., Smith, Y. E., and Van Vlack, L. H., "The MnO-MnS Phase Diagram", Trans. A.I.M.E., 1963, Vol. 227, p. 796.

15. Winegard, W. C., "Fundamentals of the Solidification of Metals", Metallurgical Reviews, 1961, Vol. 6, No. 21, p. 57.

16. Rutter, J. W., and Chalmers, B., Can. J. Physics, 1953, Vol. 31, p. 15.

17. Tiller, W. A., Jackson, K. A., Rutter, J. W., and Chalmers, B., Acta Met., 1953, Vol. 1, p. 428.

18. Smith, M. C., "Alloy Series in Physical Metallurgy", 1956, p. 90, Harper and Brothers, Publishers, New York.

19. Fick, A., Pogg. Ann., 1855, Vol. 94, p. 59.

20. Kirkaldy, J. S., Can. J. Physics, 1957, Vol. 35, p. 435.

21. Costing, L. J. and Fujita, H., J. Am. Chem. Soc., 1956, Vol. 79, p. 1099.

22. Kirkaldy, J. S., Can. J. Physics, 1958, Vol. 36, p. 899.

23. Kirkaldy, J. S., and Brown, L. C., "Diffusion Behaviour in Ternary Multiphase Systems", Can. Met. Quarterly, Jan.-March 1963, Vol. 2, No. 1, p. 89.

24. Clark, J. B., and Rhines, F. N., "Diffusion Layer Formation in the Ternary System Aluminum-Magnesium-Zinc", Trans. A.S.M., 1959, Vol. 51, p. 199.

25. Wagner, C., J. Electrochem. Soc., "Oxidation of Alloys Involving Noble Metals", 1956, Vol. 103, p. 571.

26. Kirkaldy, J. S., and Fedak, D. G., "Non-Planar Interfaces in Two-Phase Ternary Diffusion Couples", Trans. A.I.M.E., June 1962, Vol. 224, p. 490.

27. Kirkaldy, J. S., Can. J. Physics, 1958, Vol. 36, p. 917.

28. Harrison, J. D., and Wagner, C., "The Attack of Solid Alloys by Liquid Metals and Salt Melts", Acta Met., Nov. 1959, Vol. 7.

29. Cullity, B. D., "Elements of X-ray Diffraction", 1956, Addison-Wesley Publishing Co. Inc., Reading, Massachusetts, U. S. A.

30. Birks, L. S., "X-ray Spectrochemical Analysis", 1959, Interscience Publishers, Inc., New York, U. S. A.

31. Birks, L. S., "Electron Probe Microanalysis", 1963, Interscience Publishers, Inc., New York, U. S. A.

32. Castaing, R., "X-ray Microprobe Techniques", A Symposium on "X-ray Optics and X-ray Microanalysis", 1963, p. 263, Academic Press, New York, U. S. A.

33. Castaing, R., Thesis, University of Paris, 1951.

34. Castaing, R., Adv. Electron Phys., 1960, Vol. 13, p. 317.

35. Castaing, R., and Descamps, J., J. Phys. Radium, 1955, Vol. 16, p. 304.

36. Philibert, J., "A Method for Calculating the Absorption Correction in Electron-Probe Microanalysis", 1963, p. 379, Academic Press, New York, U. S. A.

37. Wittry, D. B., Thesis, California Institute of Technology, 1957.

38. Polonis, D. H., Butters, R. G., and Parr, J. G., Research, London, 1954, Vol. 7, p. 512.

39. Harris, B., and Jenkins, A. E., "Controlled Atmosphere Levitation System", J. Sci. Inst., 1959, Vol. 36, p. 258.

40. Jenkins, A. E., Harris, B., and Baker, L., "Metallurgy at High Pressures and High Temperatures", Metallurgical Society of A.I.M.E. Conference, 1963, Vol. 22, p. 25.

APPENDIX I

Determination of Optimum Counting Instrument Settings

At the start of the procedure to determine optimum settings on the counting instruments for $Fe_{K\alpha}$ radiation, the following adjustments were made:

Spectrometer angle (2θ). . . . . 33.9° (third order reflection)

Accelerating voltage . . . . . 25 KV. (approximately)

Slit width (No. 2) . . . . . 0.030 inches

Discriminator setting. . . . . 30 volts on threshold

Attenuation setting . . . . . position 1

Then as shown in Fig.19a the relationship between intensity and counter voltage setting was plotted. Selecting a counter voltage setting of 7.00 lying in the middle of the proportional region the intensity vs. threshold voltage was plotted (Fig.19b). The plateau in the curve at Q has an intensity of 3,700 counts per six seconds and the point P defined as Q/2 has an intensity of 1850 counts per six seconds. According to the instrument designers, the highest line to background ratio is obtained when P lies between 20 and 40 volts. By changing the attenuation setting to 2 and the counter voltage setting to 6.90, the whole curve was shifted to the left placing P at 30 volts (Fig.19b). After changing the discriminator settings to channel the relationship between intensity and channel height was determined for channel widths

of 2 and 4 volts (Fig.19c). The peak in the curve occurs at approximately 29.5 volts, but for best results this curve must be determined each time the instruments are used, to correct for electronic drift. The channel width giving an intensity of 90 to 95 per cent of the Q value gives the best peak to background ratio. The following summarizes the optimum settings for iron, manganese and sulphur K_{α} radiations using an accelerating voltage of approximately 25 K.V. and slit No. 2:

	Fe	Mn	S
Spectrometer angle (2θ)(degrees)	33.9	36.9	31.6
Counter voltage setting	6.90	6.93	7.31
Attenuation setting	2	2	2
Discriminator setting	channel	channel	channel
Channel height (volts)	29.5	30.0	29.0
Channel width (volts)	28	32	24

APPENDIX II

Birks'[31] Calculation of Intensities for Ternary Components

The following definitions according to Birks apply to terms in the ensuing calculations:

W_A - weight fraction of element A.

μ_{AB} - mass absorption coefficient of element A for characteristic radiation from element B.

μ'_A - total mass absorption coefficient for characteristic radiation from element A in the alloy.

μ'_{100A} - self absorption coefficient of an element for its own characteristic radiation.

ϕ - take-off angle (55°) for measuring X-rays.

F_A - intensity function for element A in the alloy.

F_{100A} - intensity function for pure element A.

I_A - X-ray intensity from element A in the alloy.

I_{100A} - X-ray intensity for pure element A.

K_F - total enhancement coefficient.

k - constant ($\simeq 0.6$).

E_{AB} - excitation efficiency for element A excited by characteristic radiation from element B.

V - electron energy in K.E.V. ($\simeq 25$).

V_{OA} - minimum excitation potential for element A in K.E.V.

P_A - atomic number correction factor for element A.

The intensity vs. weight per cent relationship will be expressed in the form of equation (20):

$$\frac{I_A}{I_{100A}} = W_A \frac{F_A}{F_{100A}} (1 + K_F) \quad .$$

It remains to calculate the intensity functions and the total enhancement coefficients for each component in the ternary system.

From Birks' tables the mass absorption coefficients can be listed as follows:

For $Mn_{K\alpha}$ Radiation	For $Fe_{K\alpha}$ Radiation	For $S_{K\alpha}$ Radiation
$\mu_{100Mn} = 93$	$\mu_{MnFe} = 74$	$\mu_{MnS} = 1,000$
$\mu_{FeMn} = 97$	$\mu_{100Fe} = 76$	$\mu_{FeS} = 1,150$
$\mu_{SMn} = 200$	$\mu_{SFe} = 170$	$\mu_{100S} = 245$

The intensity function for pure element A, F_{100A}, is calculated by determining $\mu_{100A} \cdot \csc \phi$ and reading the corresponding value from Birks' tables. Thus

$\mu_{100Mn} \cdot \csc \phi = 93\ (1.22) = 113.5$, hence $F_{100Mn} = 95.4$

$\mu_{100Fe} \cdot \csc \phi = 76\ (1.22) = 92.7$, hence $F_{100Fe} = 96.2$

$\mu_{100S} \cdot \csc \phi = 245\ (1.22) = 299.0$, hence $F_{100S} = 83.4$.

The intensity function for element A in the alloy, F_A, is found by calculating the total absorption coefficient μ'_A, determining $\mu'_A \cdot \csc \phi \cdot P_A$ and reading the corresponding value from Birks' tables. Thus for a ternary alloy of the following composition:

Mn -- 40%

Fe -- 30%

S -- 30%

$$\mu'_{Mn} = W_{Mn}(\mu_{100Mn}) + W_{Fe}(\mu_{FeMn}) + W_S(\mu_{SMn}) = 126.3$$

$$\mu'_{Mn} \csc \phi \; P_{Mn} = (126.3)(1.22)(1.0) = 154, \quad \text{hence } F_{Mn} = 93.7$$

$$\mu'_{Fe} = W_{Mn}(\mu_{MnFe}) + W_{Fe}(\mu_{100Fe}) + W_S(\mu_{SFe}) = 103.4$$

$$\mu'_{Fe} \csc \phi \; P_{Fe} = (103.4)(1.22)(1.0) = 126, \quad \text{hence } F_{Fe} = 94.9$$

$$\mu'_S = W_{Mn}(\mu_{MnS}) + W_{Fe}(\mu_{FeS}) + W_S(\mu_{100S}) = 819$$

$$\mu'_S \csc \phi \; P_S = (819)(1.22)(1.07) = 1070, \quad \text{hence } F_S = 66.0$$

The total enhancement coefficient K_F is given by an equation of the form

$$K_F = k \; E_{AB} \left(\frac{\mu_{AB}}{\mu'_B}\right) \cdot \left(\frac{V - V_{OB}}{V - V_{OA}}\right)^2$$

where K_F is the contribution from $B_{K\alpha}$ radiation to the $A_{K\alpha}$ radiation.

For $Mn_{K\alpha}$ radiation excited by $Fe_{K\alpha}$, $K_F = 0$ because $E_{MnFe} = 0$.

For $Mn_{K\alpha}$ radiation excited by $S_{K\alpha}$, $K_F = 0$ because $E_{MnS} = 0$.

For $Fe_{K\alpha}$ radiation excited by $Mn_{K\alpha}$, $K_F = 0$ because $E_{FeMn} = 0$.

For $Fe_{K\alpha}$ radiation excited by $S_{K\alpha}$, $K_F = 0$ because $E_{FeS} = 0$.

For $S_{K\alpha}$ radiation excited by $Mn_{K\alpha}$

$$K_F = (0.6)(0.026) \; W_{Mn} \left(\frac{200}{\mu'_{Mn}}\right) \left(\frac{25 - 6.5}{25 - 2.5}\right)^2 = 2.11 \left(\frac{W_{Mn}}{\mu'_{Mn}}\right) = 0.00667$$

For $S_{K\alpha}$ radiation excited by $Fe_{K\alpha}$

$$K_F = (0.6)(0.022)\, W_{Fe} \left(\frac{170}{\mu'_{Fe}}\right) \left(\frac{25 - 7.1}{25 - 2.5}\right)^2 = 1.42 \left(\frac{W_{Fe}}{\mu'_{Fe}}\right) = 0.00412 \quad .$$

The total enhancement coefficient for $S_{K\alpha}$ excited by $Mn_{K\alpha}$ and $Fe_{K\alpha}$ radiations is given by

$$K_{F_{(S)}} = 0.0067 + 0.00412 = 0.0108 \quad .$$

The intensities for each of the ternary components can now be expressed according to equation (20):

$$\frac{I_{Mn}}{I_{100Mn}} = 0.4 \left(\frac{93.7}{95.4}\right) (1) = 0.393$$

$$\frac{I_{Fe}}{I_{100Fe}} = 0.3 \left(\frac{94.9}{96.2}\right) (1) = 0.296$$

$$\frac{I_S}{I_{100S}} = 0.3 \left(\frac{66.0}{88.4}\right) (1 + 0.0108) = 0.226$$

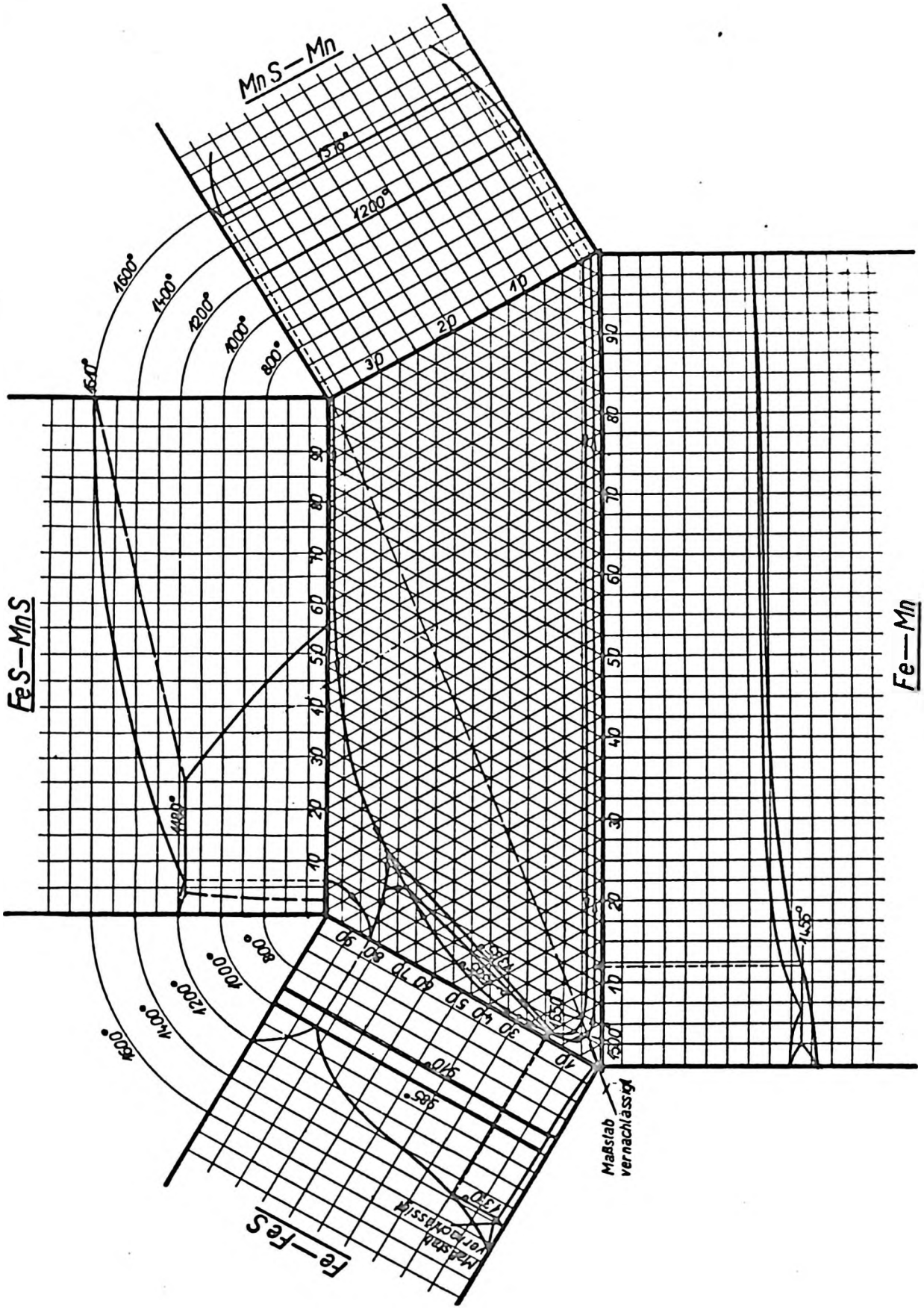

Fig. 1 The ternary system proposed by Wentrup[9].

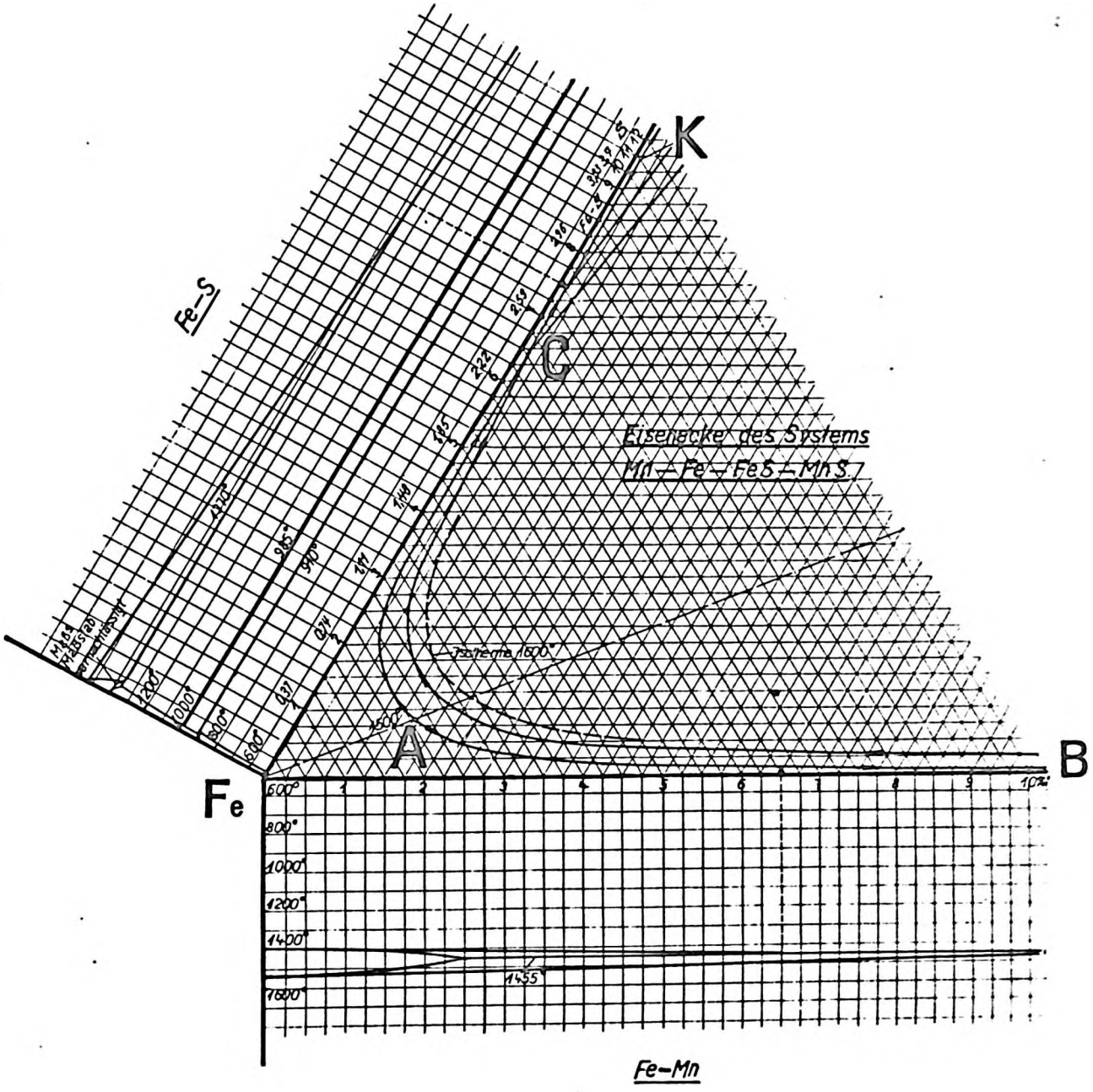

Fig. 1a The iron-rich corner of the Fe-Mn-S system proposed by Wentrup[9].

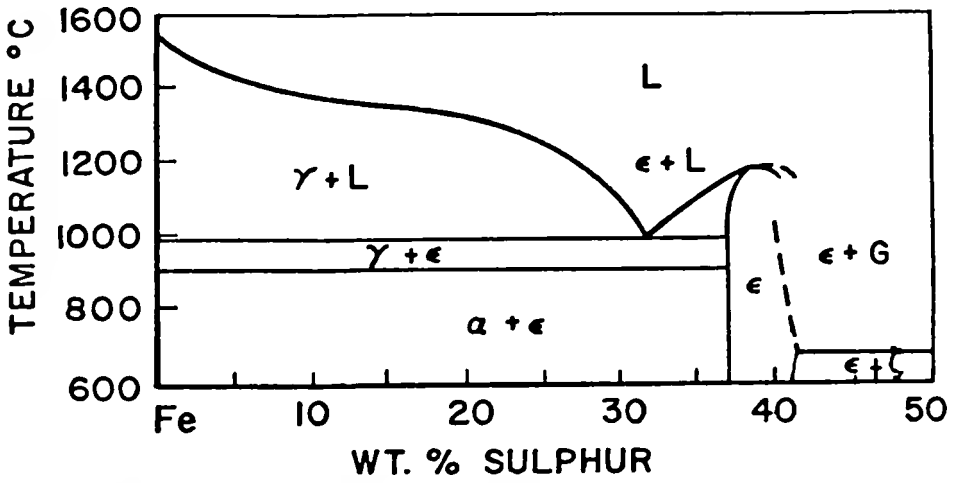

Fig. 2 The Fe-FeS system according to Chipman[10].

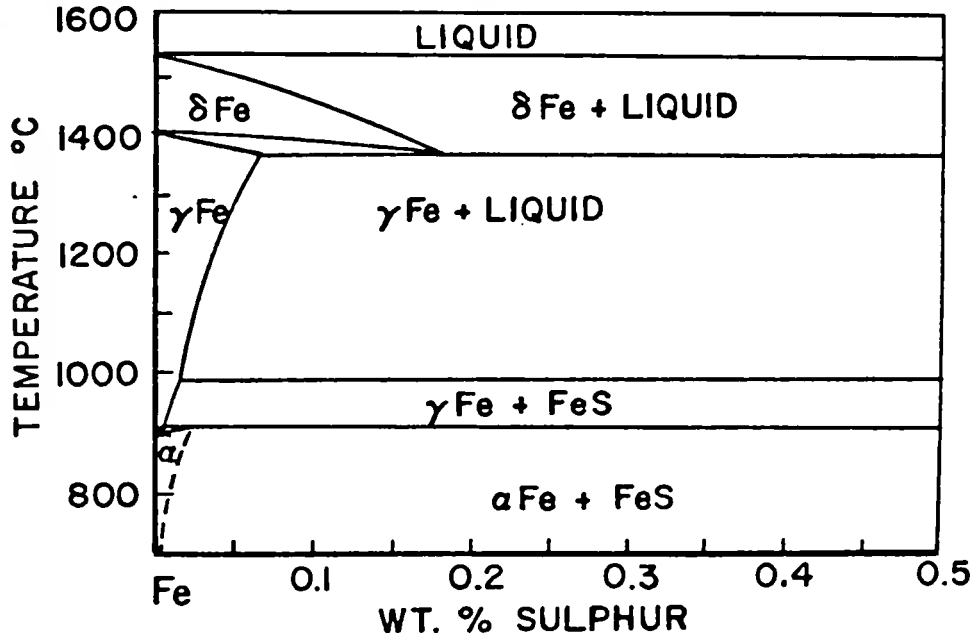

Fig. 3 The solid solubilities of sulphur in high purity iron as determined by Rosenquist and Dunicz[12].

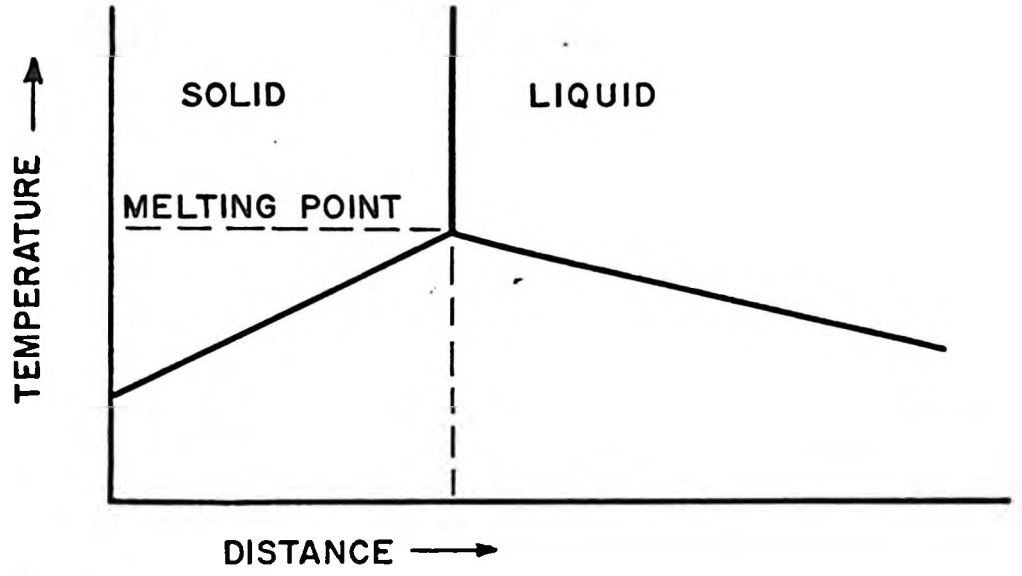

Fig. 4 A negative temperature gradient in pure liquid metal during unidirectional solidification.

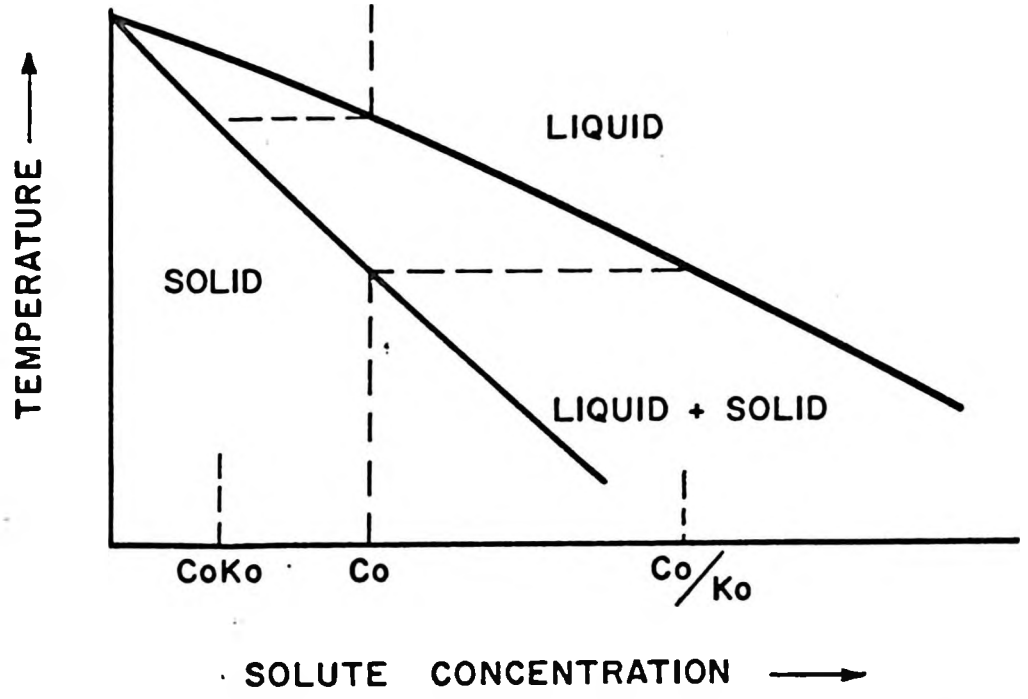

Fig. 5 The freezing of a simple binary alloy of composition C_o where the distribution coefficient, K_o, is less than one.

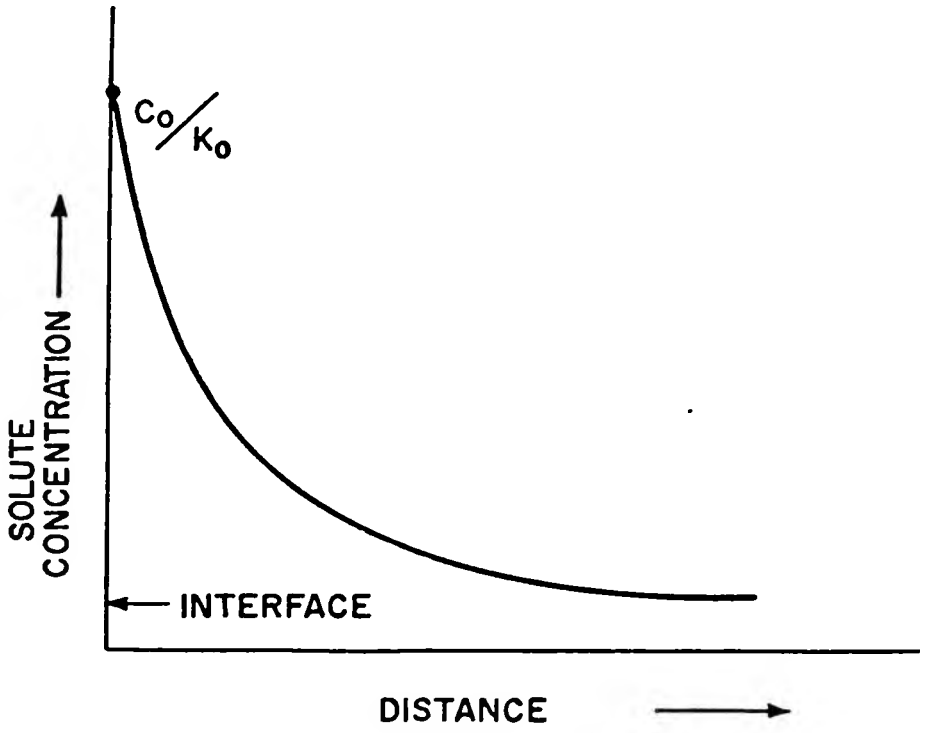

Fig. 6 A decreasing exponential solute distribution in the liquid ahead of the solid-liquid interface.

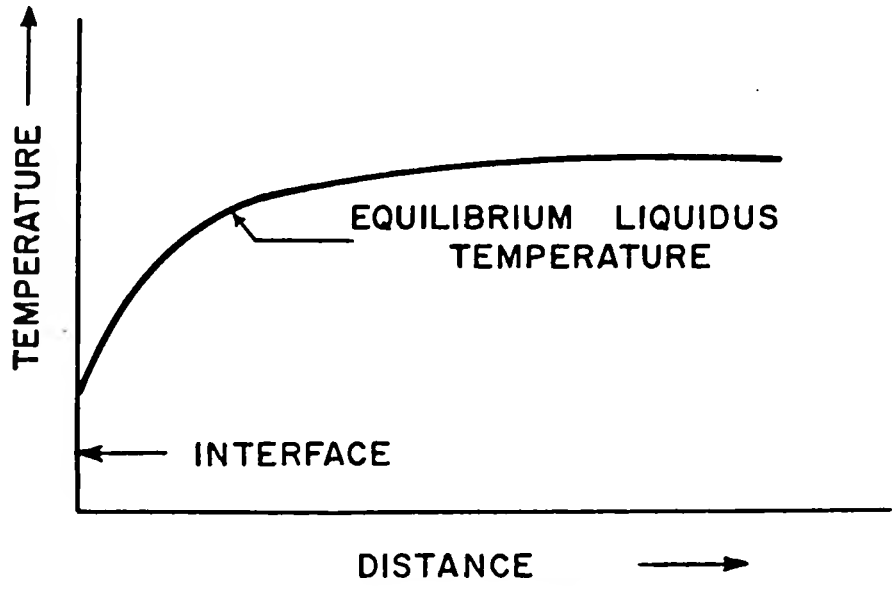

Fig. 7 The distribution of equilibrium freezing temperature determined by the liquidus line of the phase diagram.

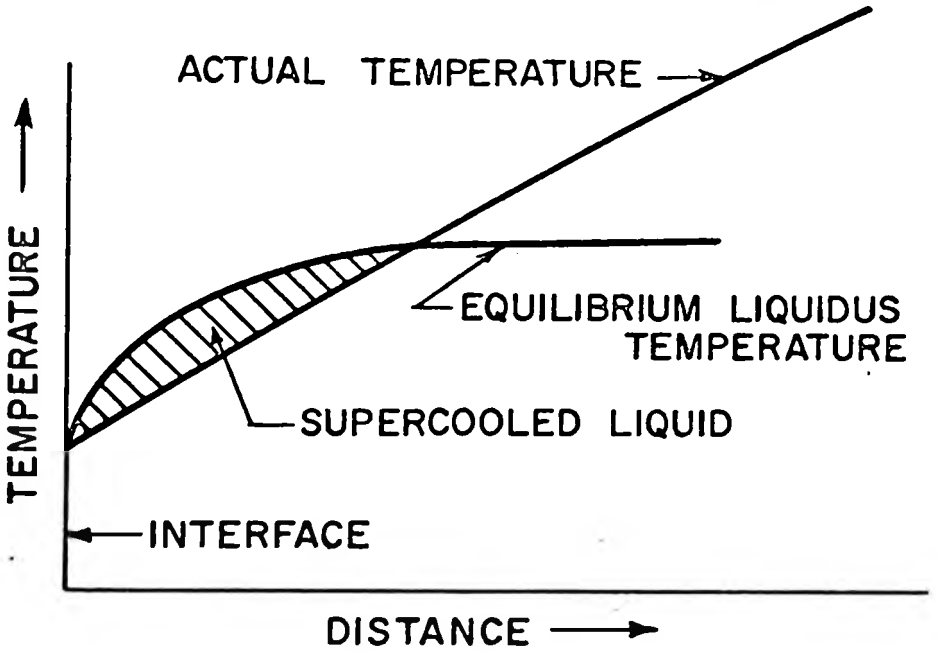

Fig. 8 A zone of supercooled liquid in front of the solid-liquid interface.

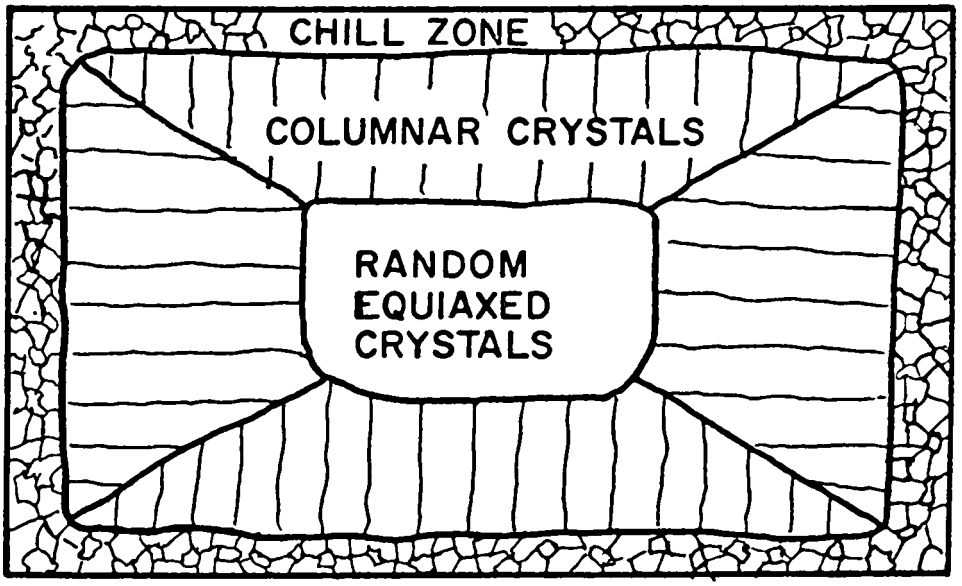

Fig. 9 The three zones of grain structure in the cross-section of an alloy ingot.

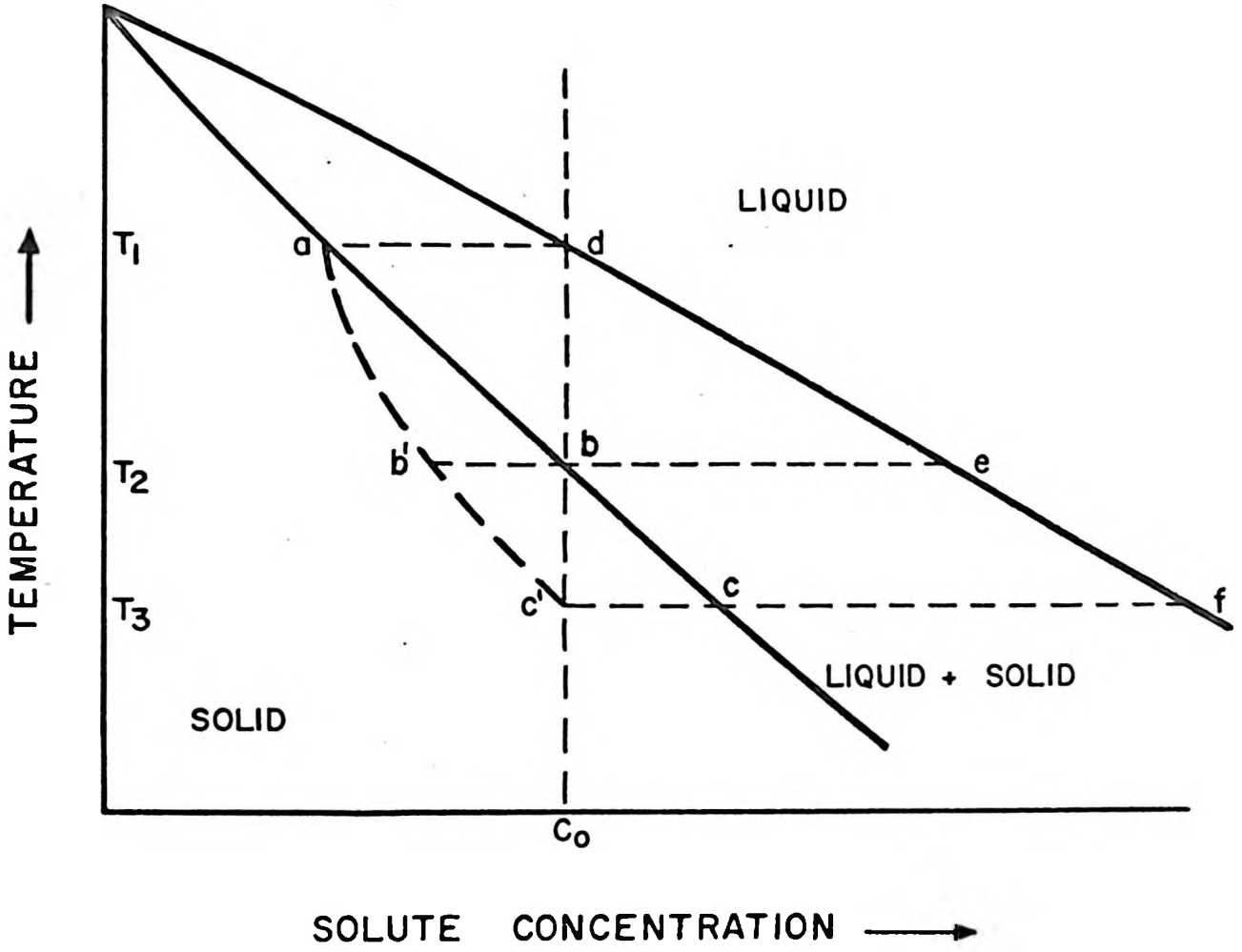

Fig. 10 Coring in a simple binary alloy of composition C_o.

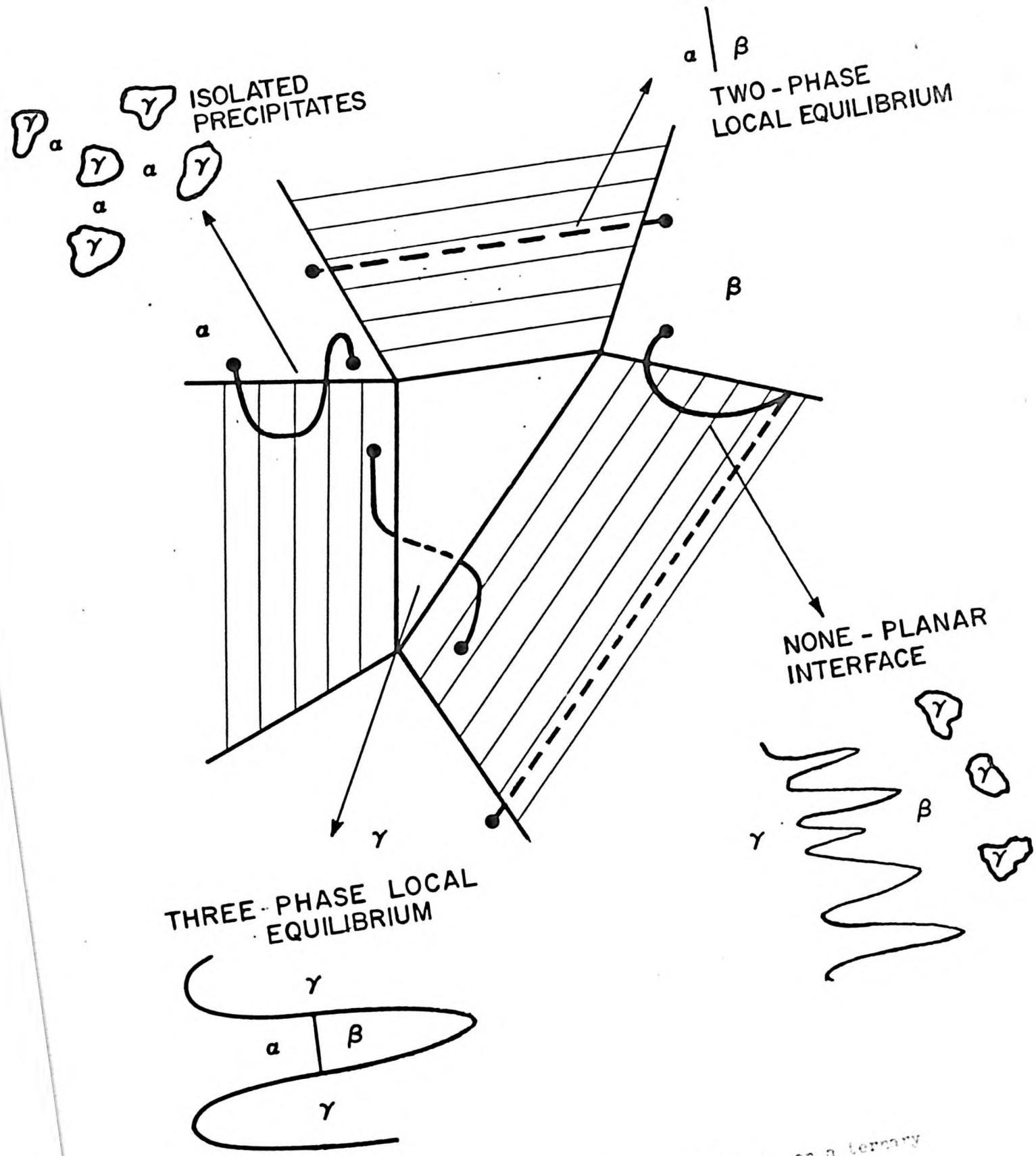

Fig. 11 A schematic drawing of diffusion paths on a ternary isotherm and the related micro-structures in a diffusion couple.

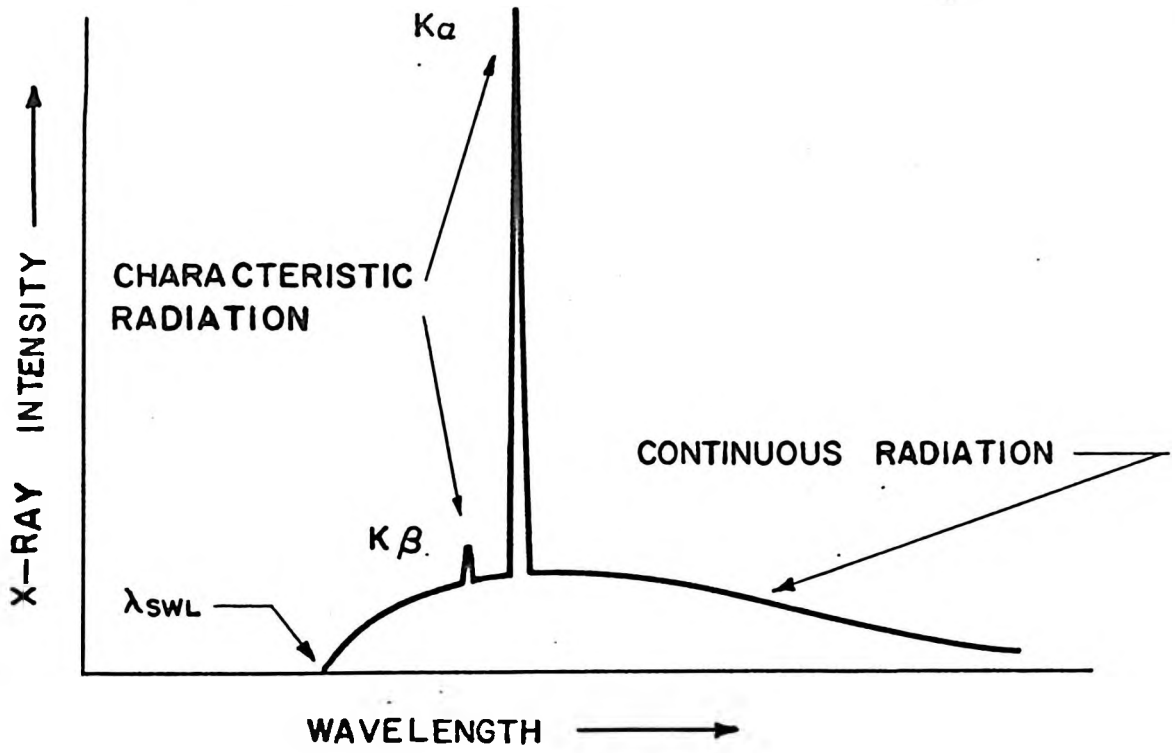

Fig. 12 Schematic X-ray spectrum of an element excited at a typical accelerating voltage in an electron probe.

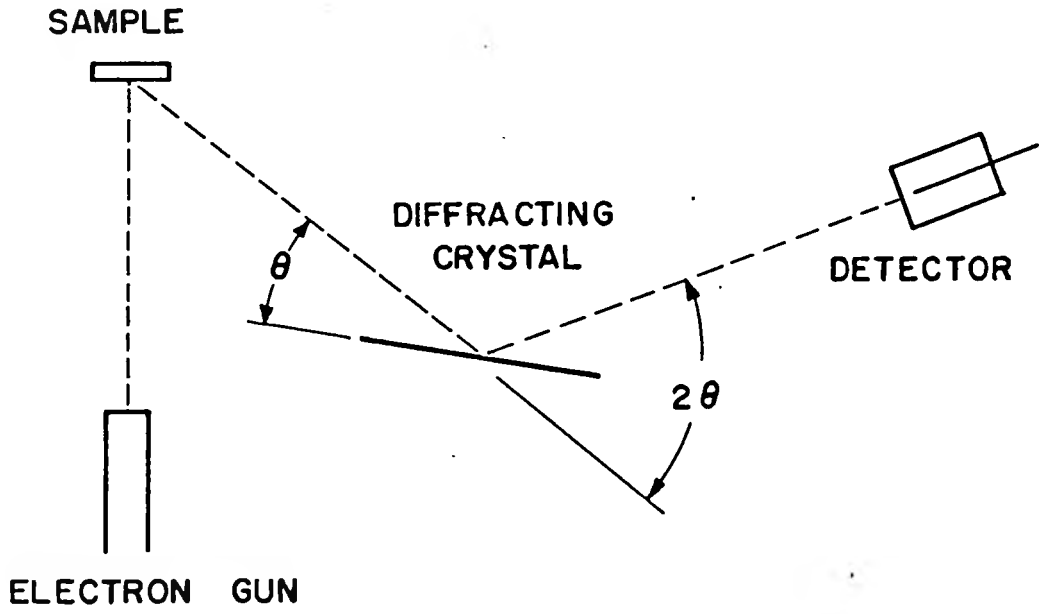

Fig. 13 Schematic representation of an X-ray path between a sample, a diffracting crystal and a detector in an electron probe.

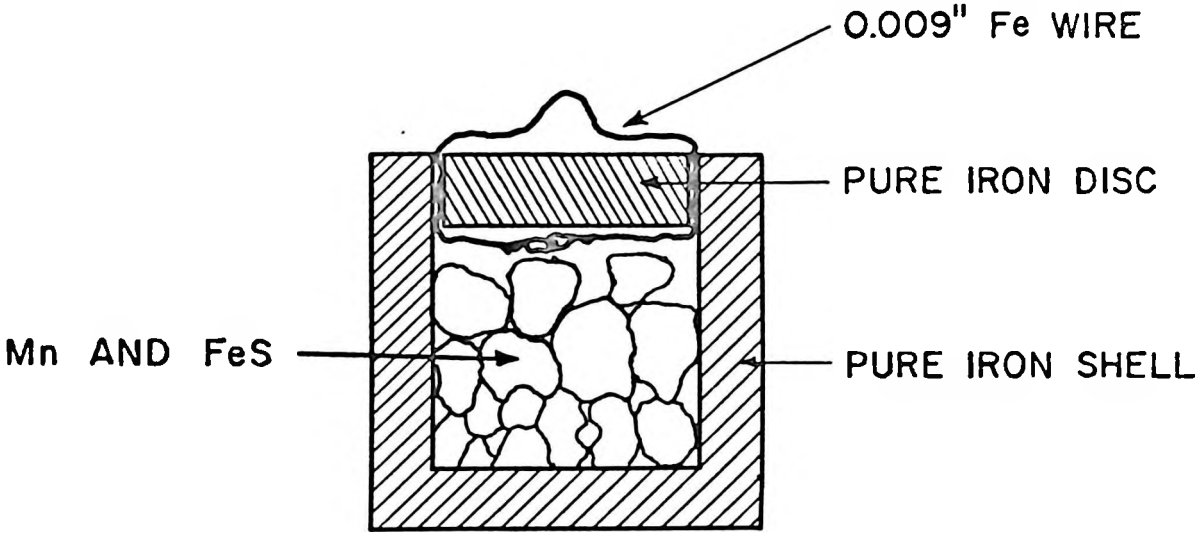

Fig. 1-a Schematic cross-section of a sample ready for levitation.

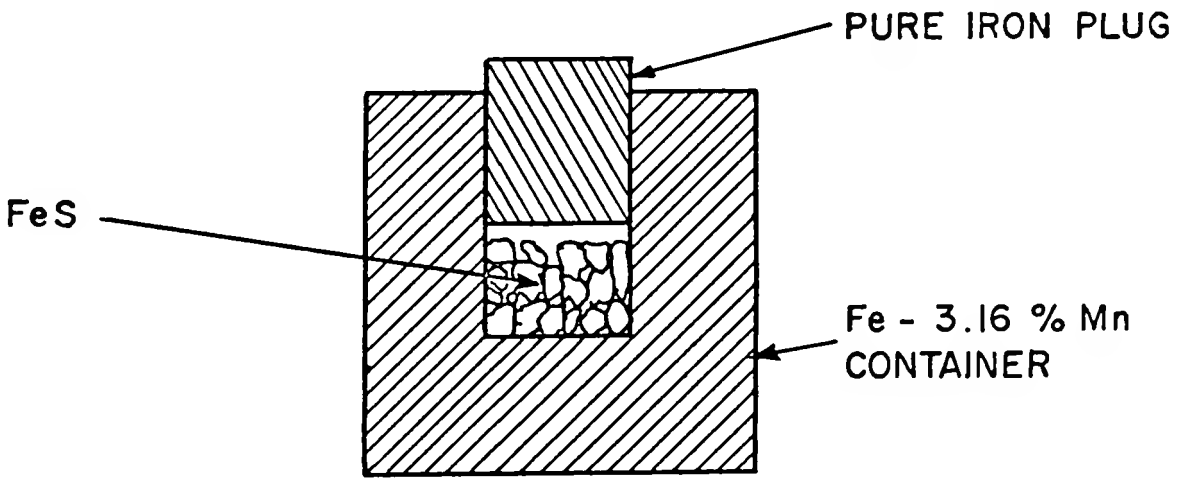

Fig. 1-b Schematic cross-section of a finite diffusion couple ready for high frequency heating.

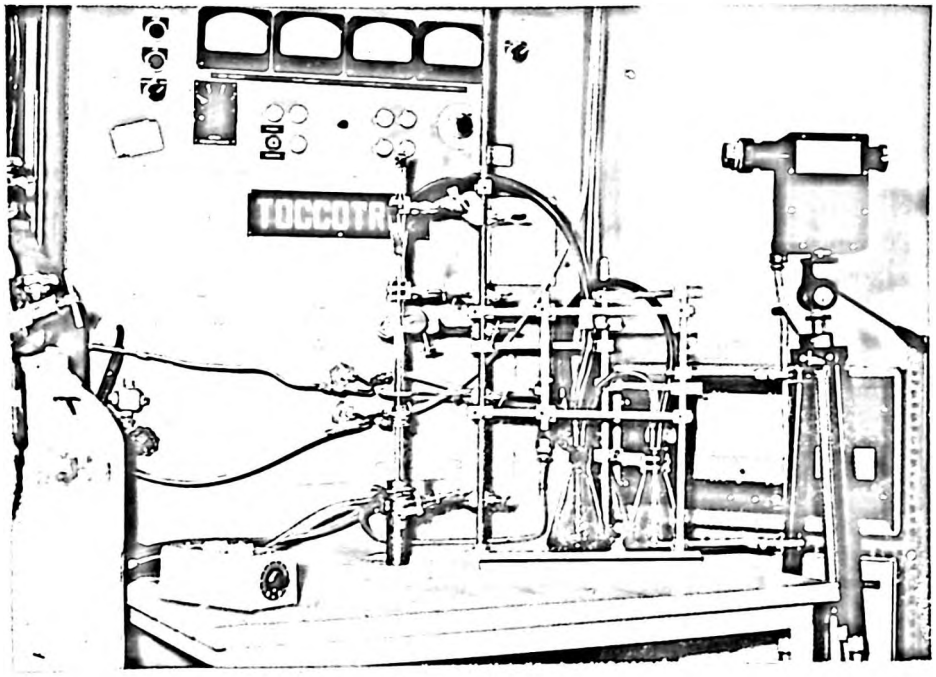

Fig. 15 Photograph of the levitation apparatus.

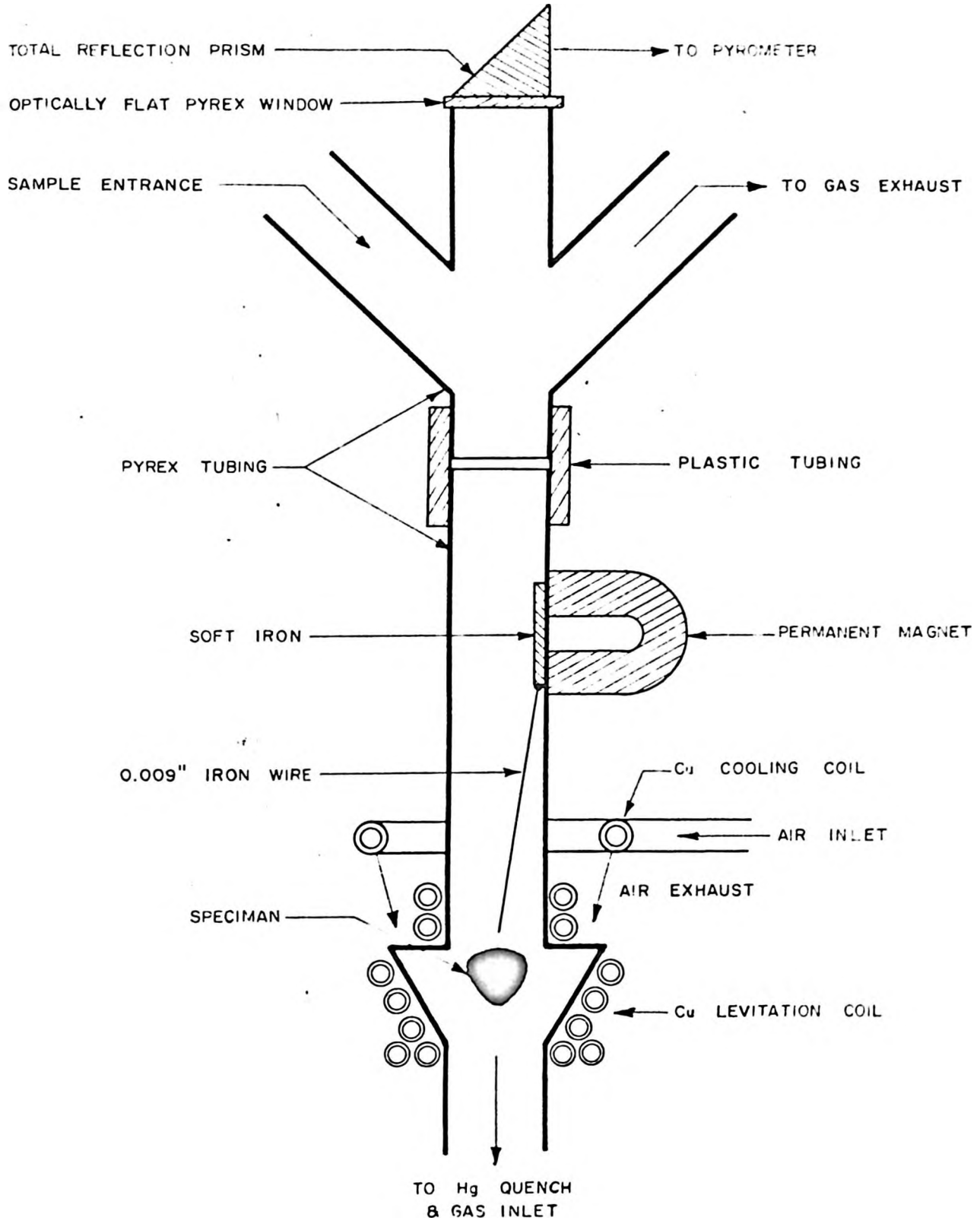

Fig. 16 Schematic cross-section through the levitation apparatus.

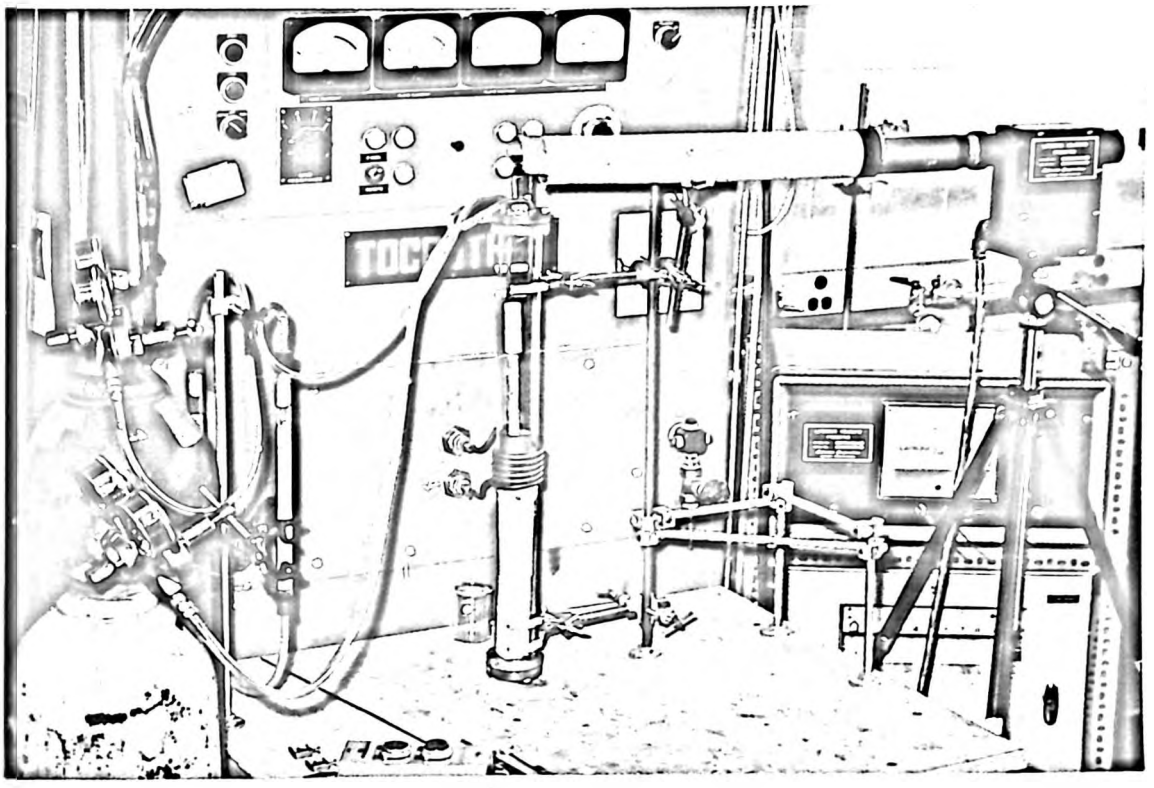

Fig. 17 Photograph of the high frequency heating apparatus.

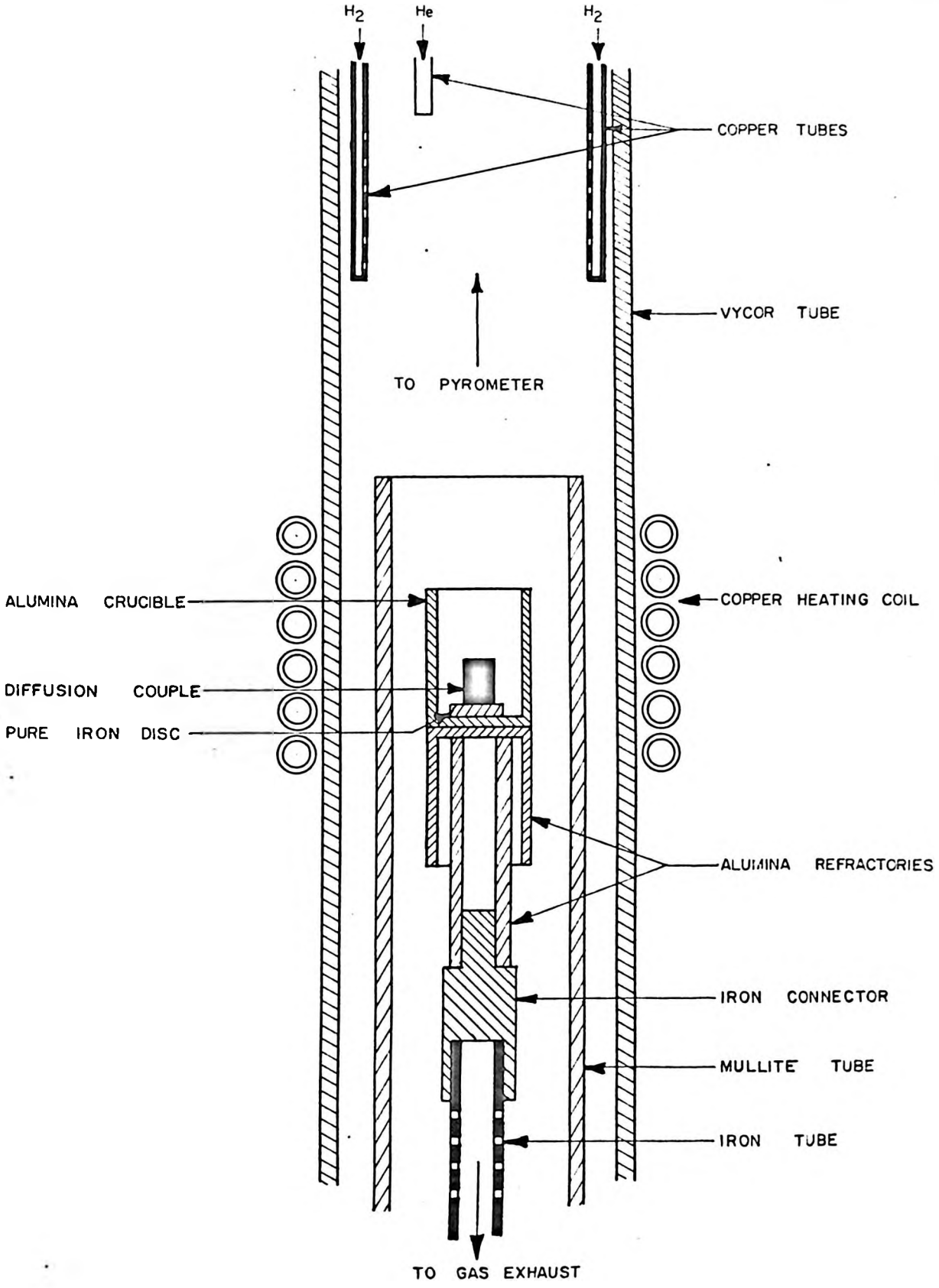

Fig. 18 Schematic cross-section through the high frequency heating apparatus.

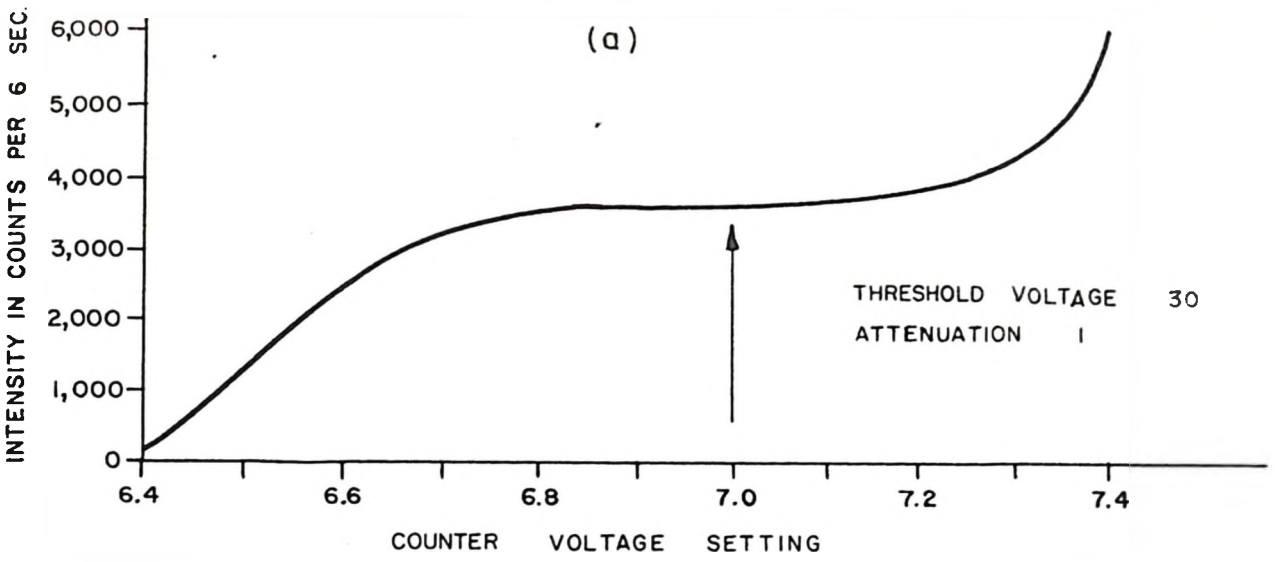

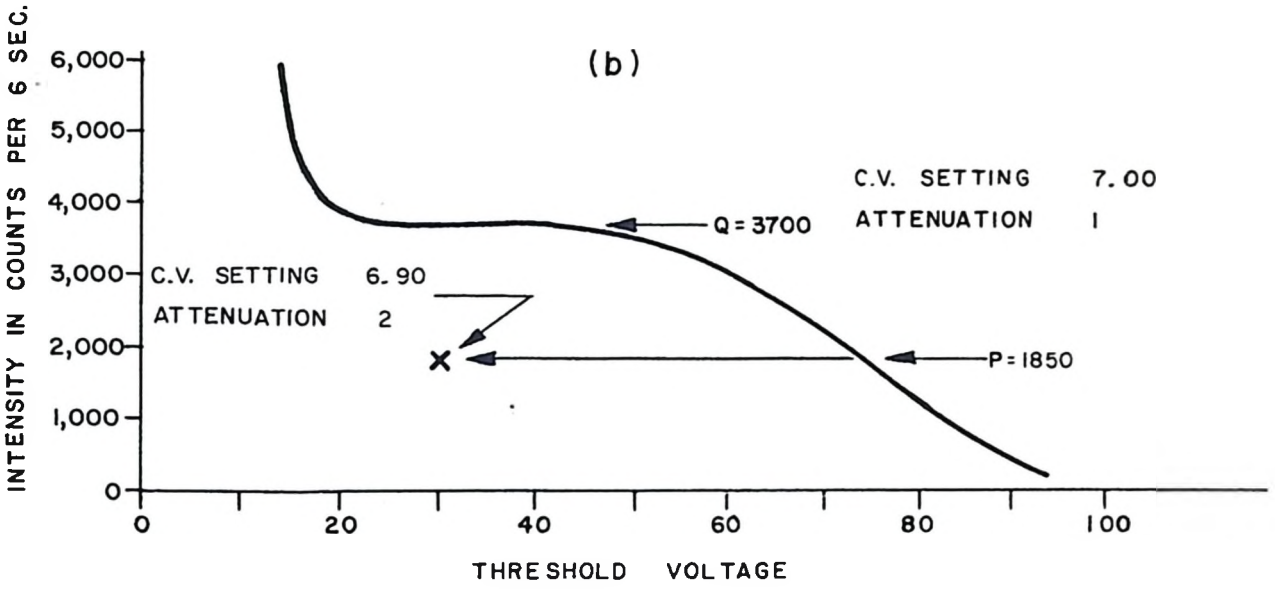

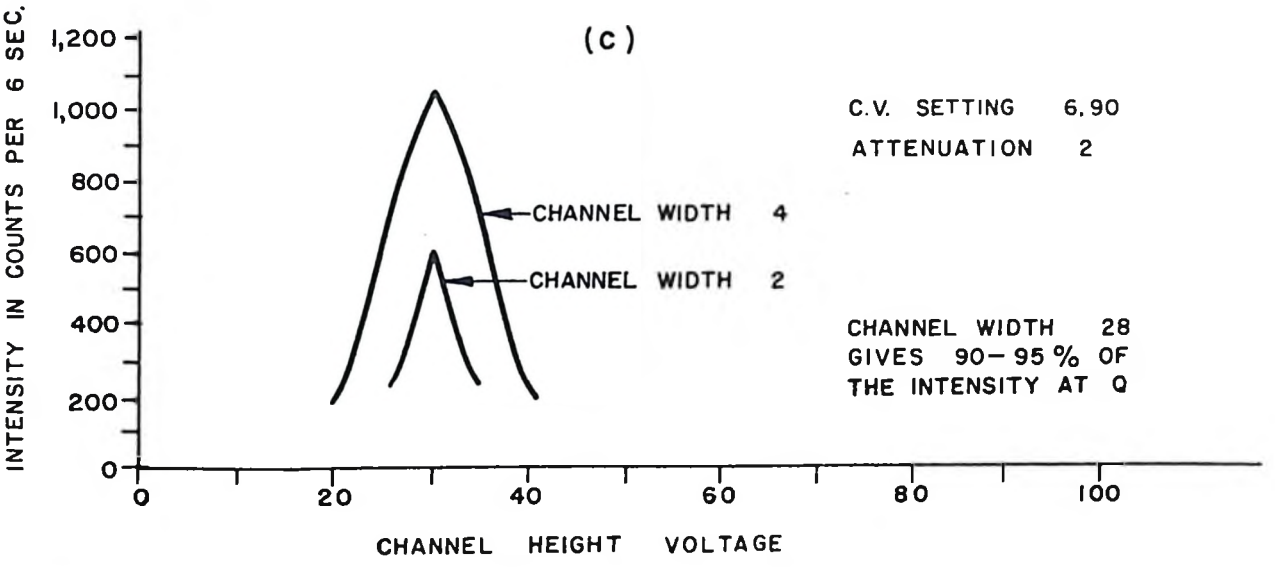

Fig. 19 Plots of x_{K_α} intensity vs. (a) counter voltage setting, (b) threshold voltage, (c) channel width voltage. The accelerating voltage was 25 K..., the slit [illegible] and the take-off angle was [illegible]. Other settings are as shown.

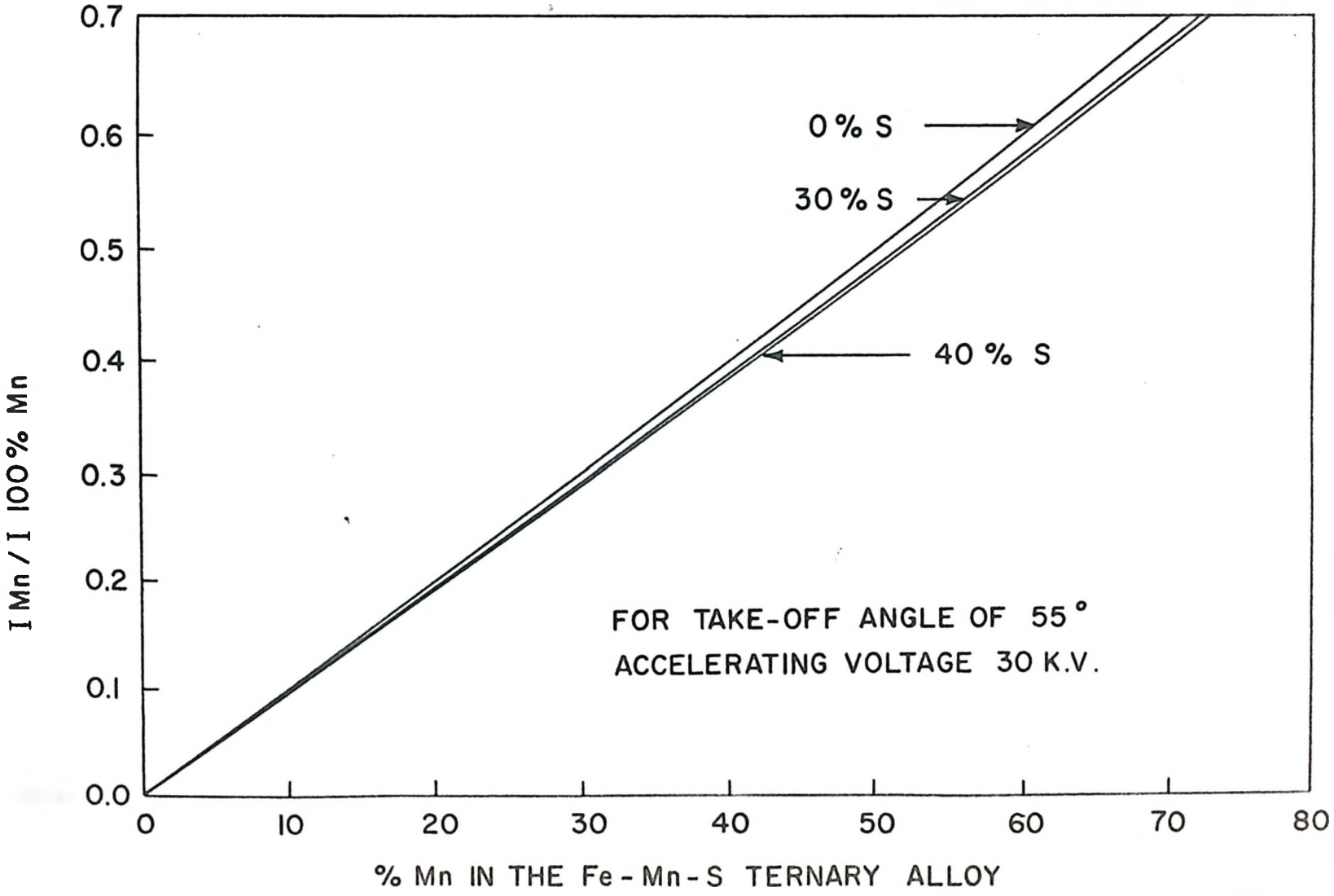

Fig. 20 Calibration curve for Mn in Fe-Mn-S ternary alloy using the 3rd order $Mn_{K\alpha}$ line.

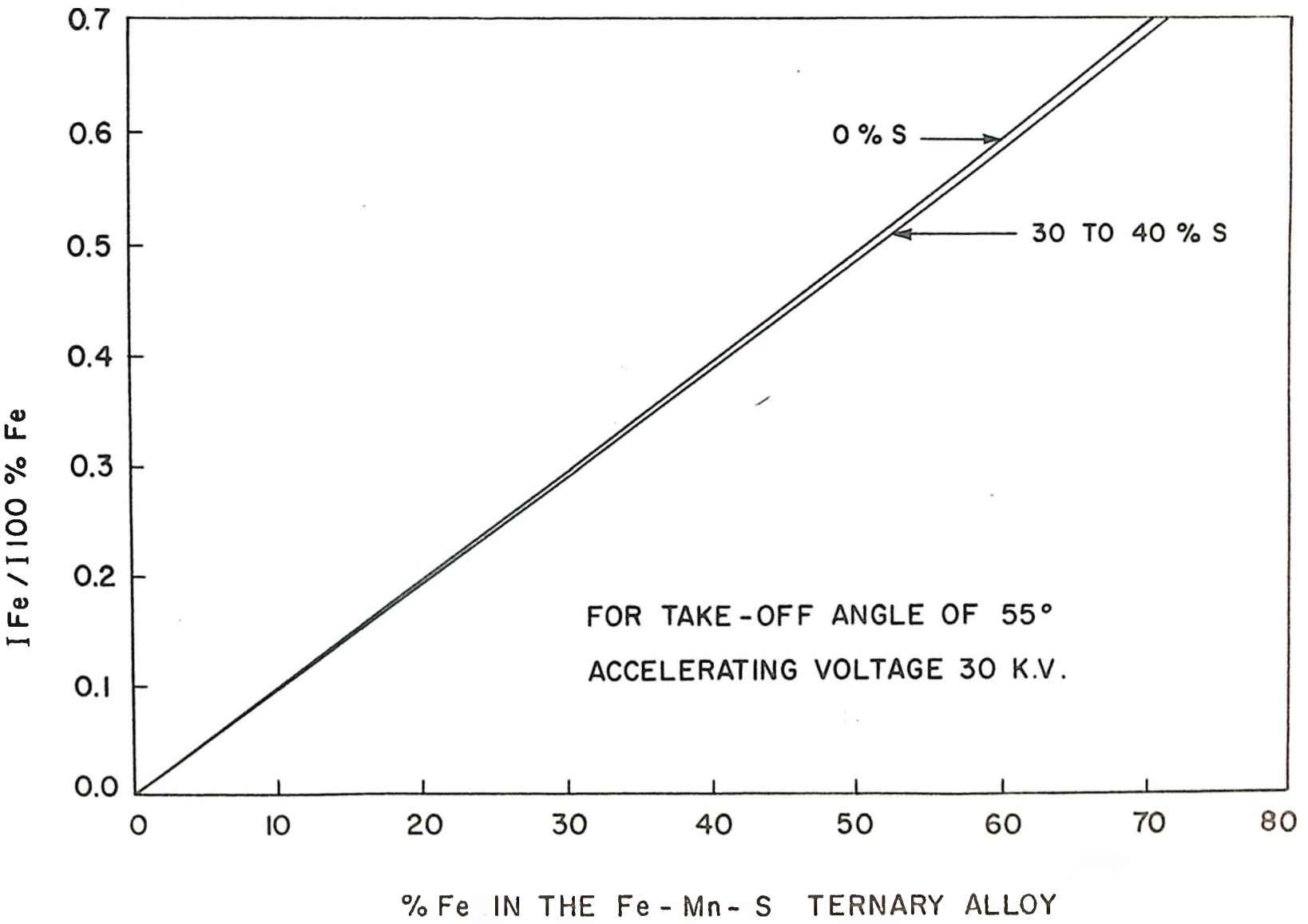

Fig. 21 Calibration curve for Fe in Fe-Mn-S ternary alloy using the 3rd order $Fe_{K\alpha}$ line.

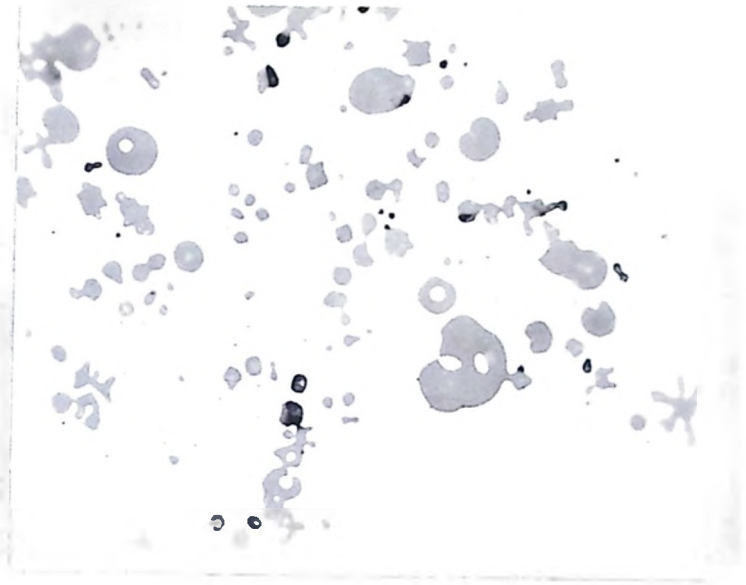

Fig. 22 Photo showing typical βMn3 inclusions near the surface of a levitated specimen. Note the precipitates and fingers of iron in the sulphides. 800x

Fig. 23 Photo of a cross-section through the bottom half of a levitated specimen encased in a sulphide film. 14x

Fig. 24 Typical βMnS film on the surface of a levitated specimen. Note the iron precipitates and the non-planar sulphide-iron interface. 800x

Fig. 25 Photomicrograph of αFeS-βMnS inclusions in a levitated specimen quenched from about 1535°C. 2250x

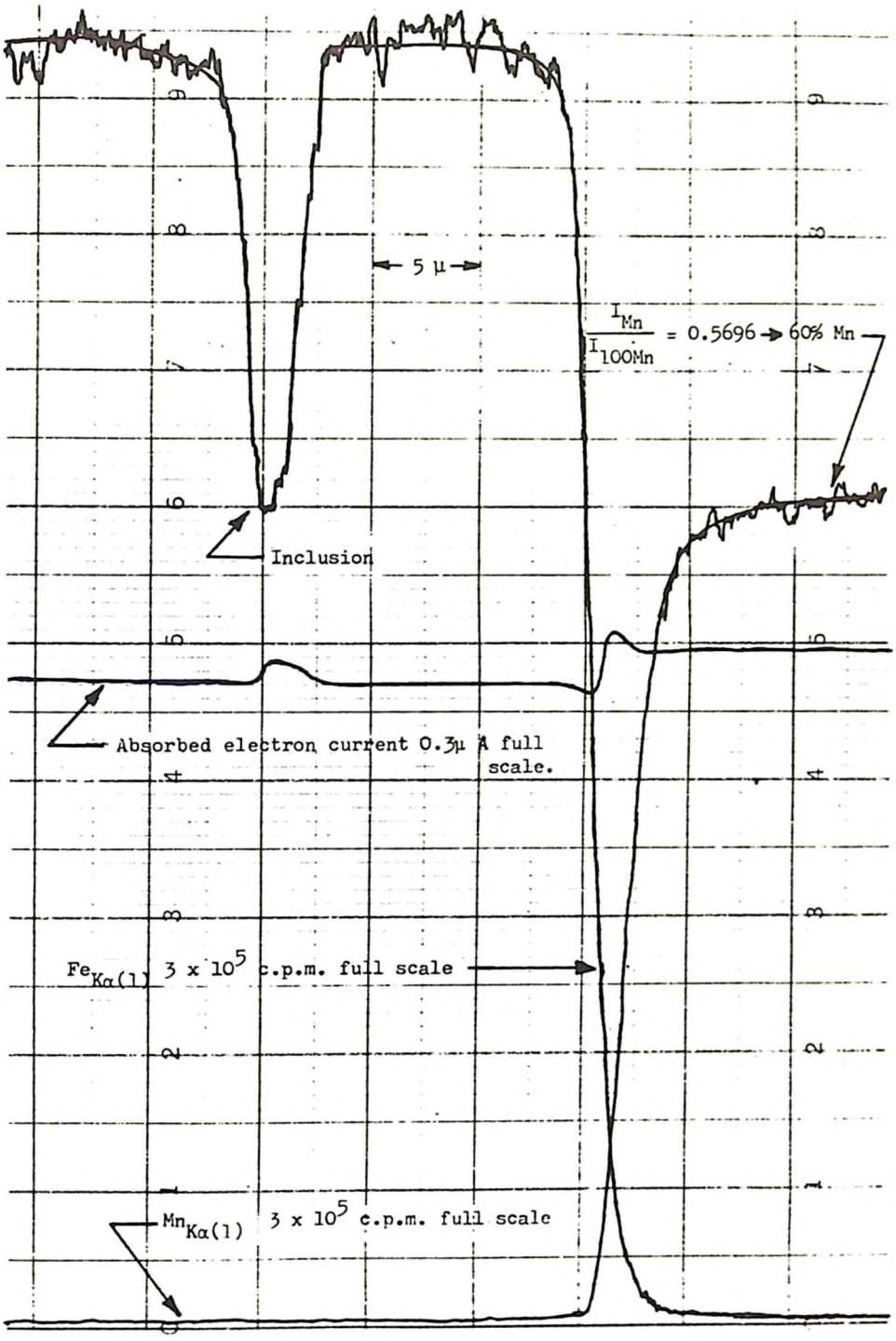

Fig. 26 A reproduction of strip chart from the Fisher probe showing X-ray intensity of $Fe_{K\alpha(1)}$ and $Mn_{K\alpha(1)}$ across a typical sulphide film-iron interface of a levitated specimen.

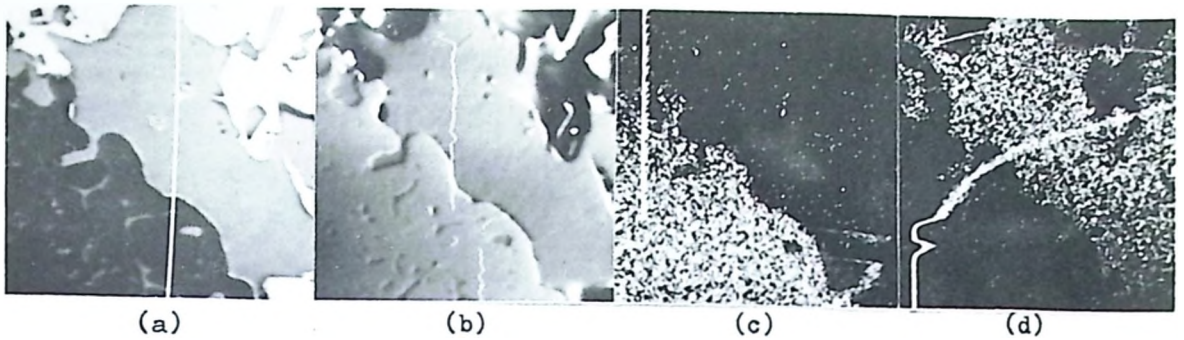

(a) (b) (c) (d)

Fig. 27 Scanning images on a 90μ square cross-section at the sulphide film - iron interface of a levitated specimen, (a) absorbed electron image and absorbed electron path, (b) electron backscatter image showing the surface topography, (c) X-ray image of Fe, (d) X-ray image of S.

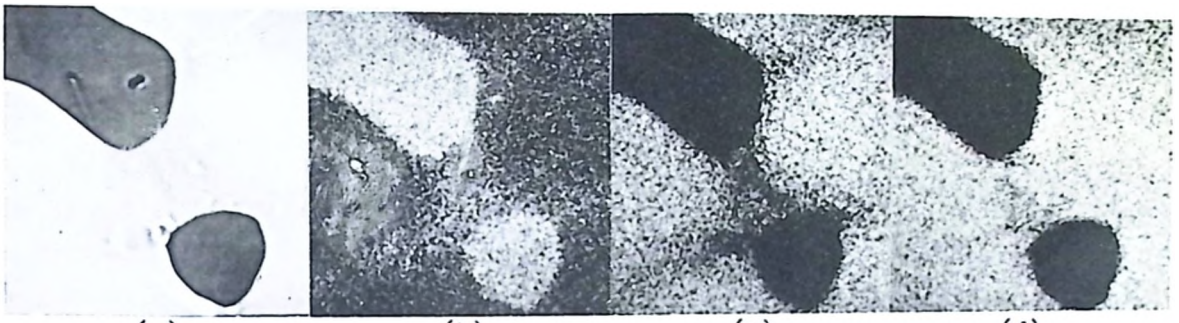

(a) (b) (c) (d)

Fig. 32 Scanning images on a 90μ square cross-section through the center of a Battelle iron pot (No. 8) equilibrated with FeS and βMnS, (a) absorbed electron image, (b) X-ray image of Fe, (c) X-ray image of Mn, (d) X-ray image of S.

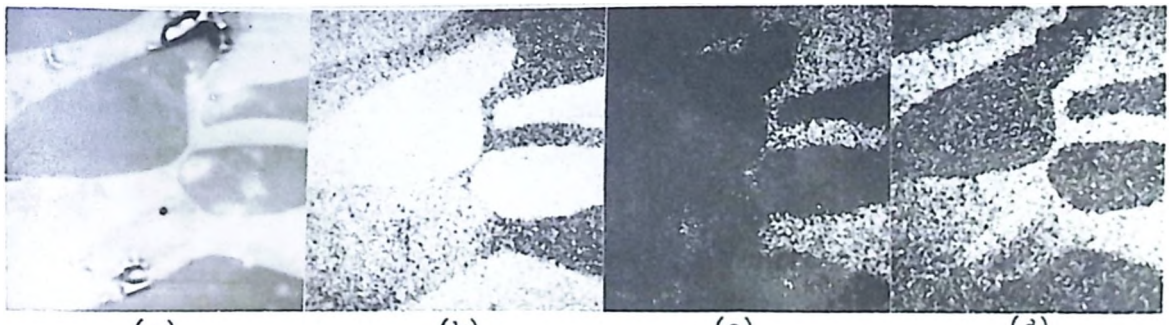

(a) (b) (c) (d)

Fig. 33 Scanning images on a 90μ square cross-section through the center of a Battelle iron pot (No. 10) equilibrated with FeS and βMnS, (a) absorbed electron image, (b) X-ray image of Fe, (c) X-ray image of Mn, (d) X-ray image of S.

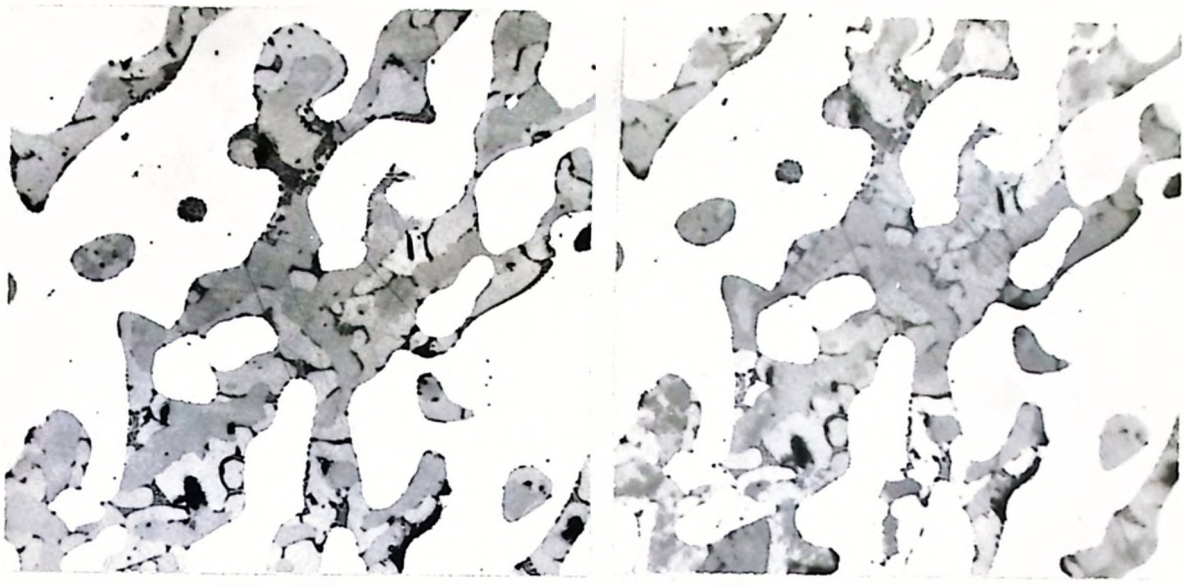

(a) Blue Filter (b) Polarized Light

Fig. 28 Photos showing the light grey FeS and the darker grey βMnS equilibrated with a Pure Iron pot. Under polarized light the boundaries between the two sulphides are not clearly defined. Note the very dark grey eutectic oxide. 750x

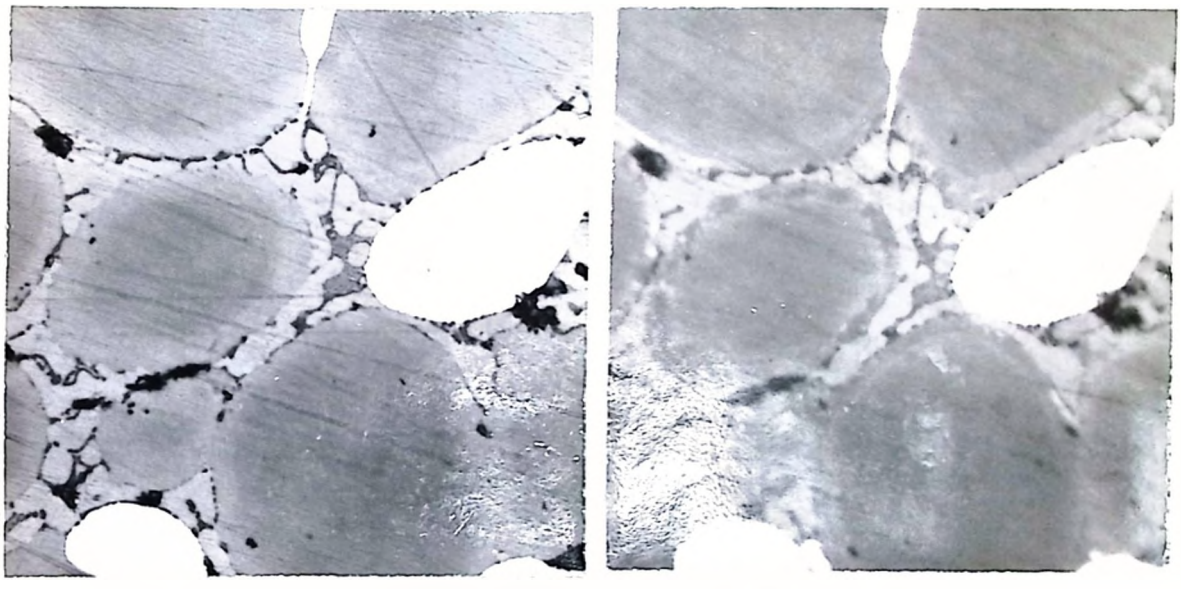

(a) Blue Filter (b) Polarized Light

Fig. 29 Photos showing the greater extent of the FeS and βMnS phases formed in the Battelle iron containers. Note the intermediate grey colour of the phase mixture between the two sulphide phases and also the very dark grey eutectic oxide. 750x

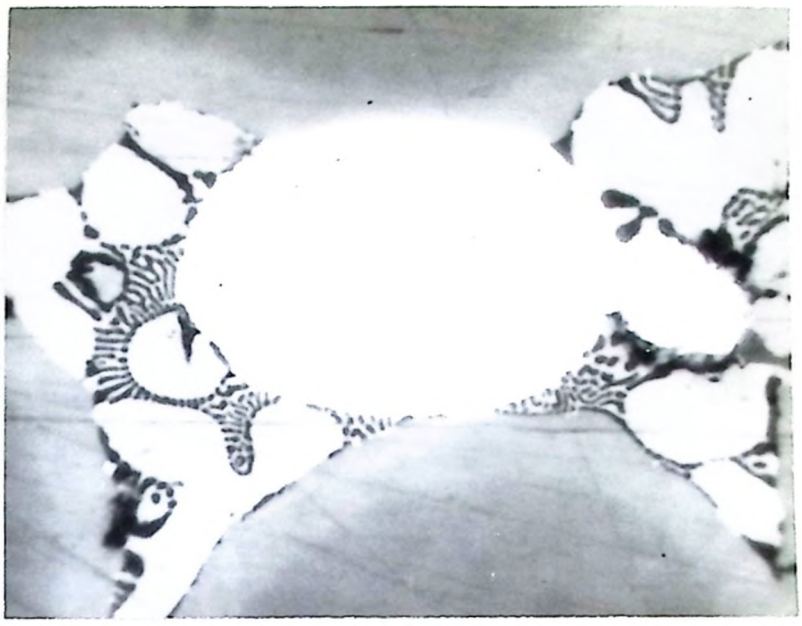

(a) Blue Filter

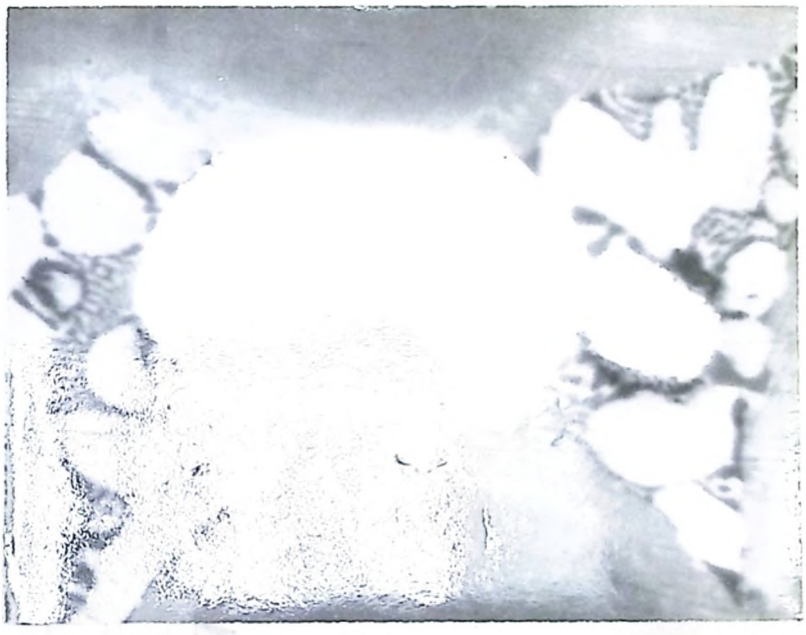

(b) Polarized Light

Fig. 30 Photos showing the phase mixture between the two sulphide phases. 2250x

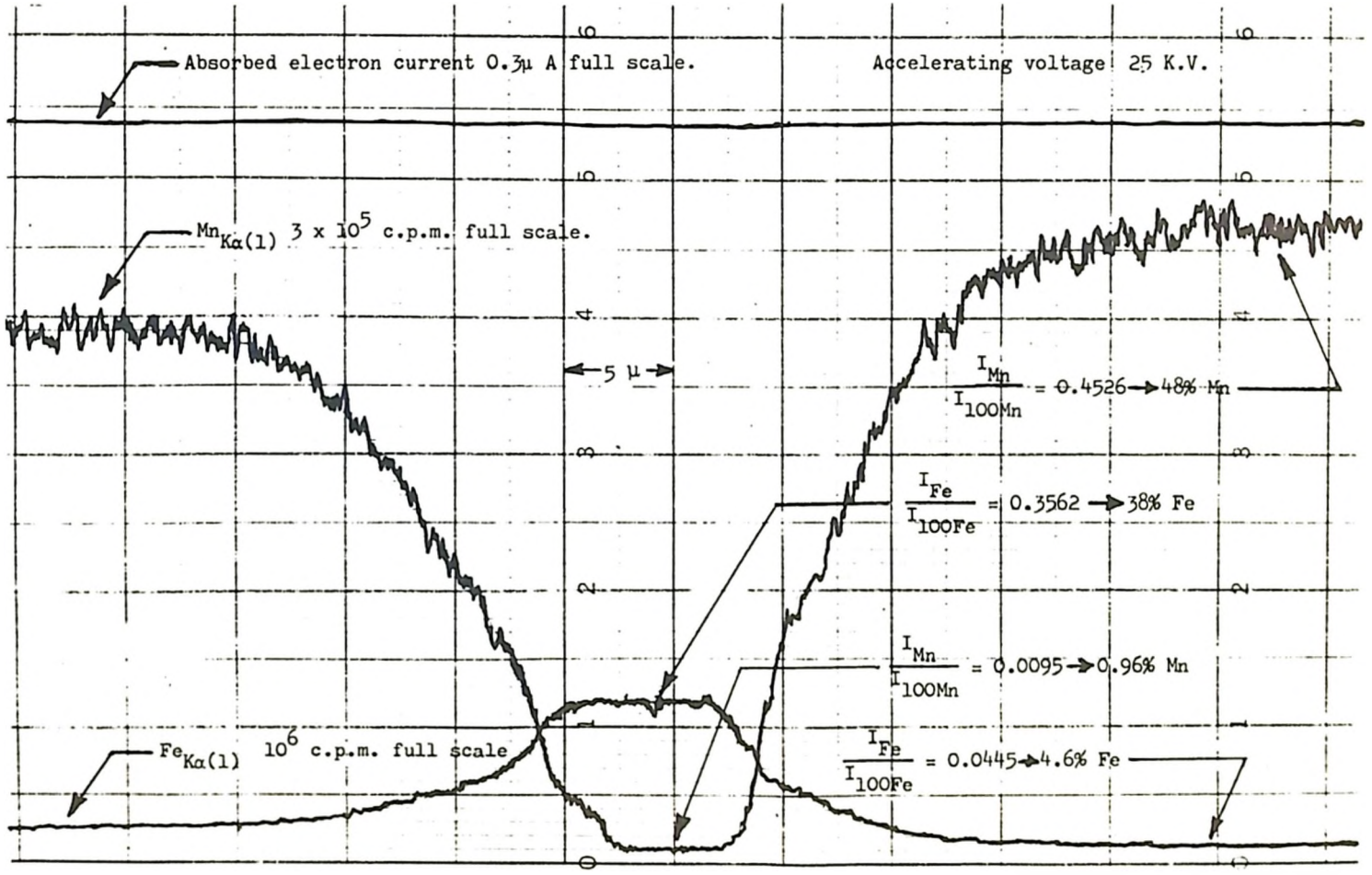

Fig. 31 A reproduction of strip chart from the Fisher probe showing X-ray intensities of $Fe_{K\alpha(1)}$ and $Mn_{K\alpha(1)}$ between βMnS and αFeS phases at a distance of approximately 10μ from an iron phase.

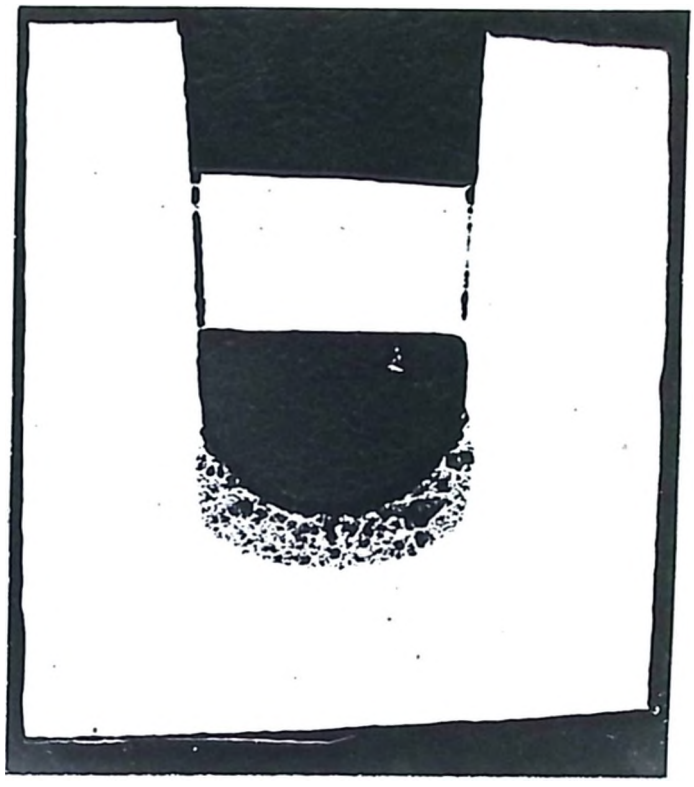

Fig. 34 A cross-section of a diffusion couple showing the sulphide retained in a Fe - 3.16% Mn container by a short Pure Iron plug. 14x

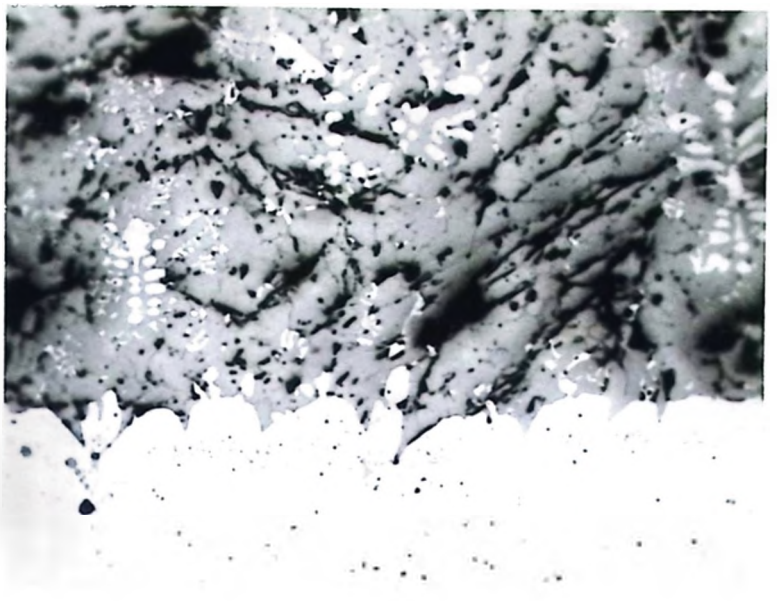

(a)

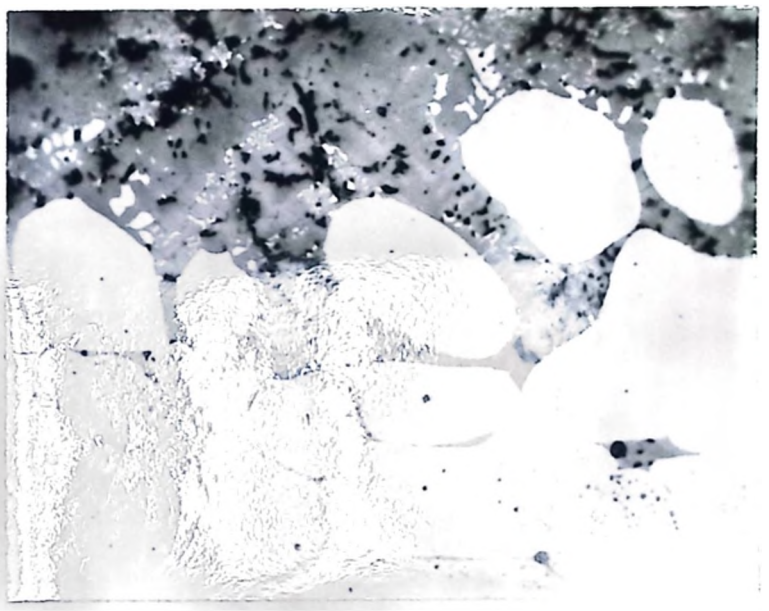

(b)

Fig. 35 Photomicrographs showing iron intrusions in (a) FeS after 10 minutes at 1300°C, (b) FeS equilibrated with βMnS after 80 minutes at 1300°C. Note the fine precipitates at the front of the sulphide - iron interface. 600x

Fig. 36 Photomicrograph of the large areas of iron between the αFe_3-βMnS phases equilibrated at 1300°C for 80 minutes. Note the fine precipitates at the front of the sulphide-iron interface. 800x, Polarized Light

Fig. 37 Photomicrograph of the fine precipitates at the front of the sulphide-iron interface. Note that some precipitates have a very dark phase at the surface while others have iron in the core. 2250x, Polarized Light

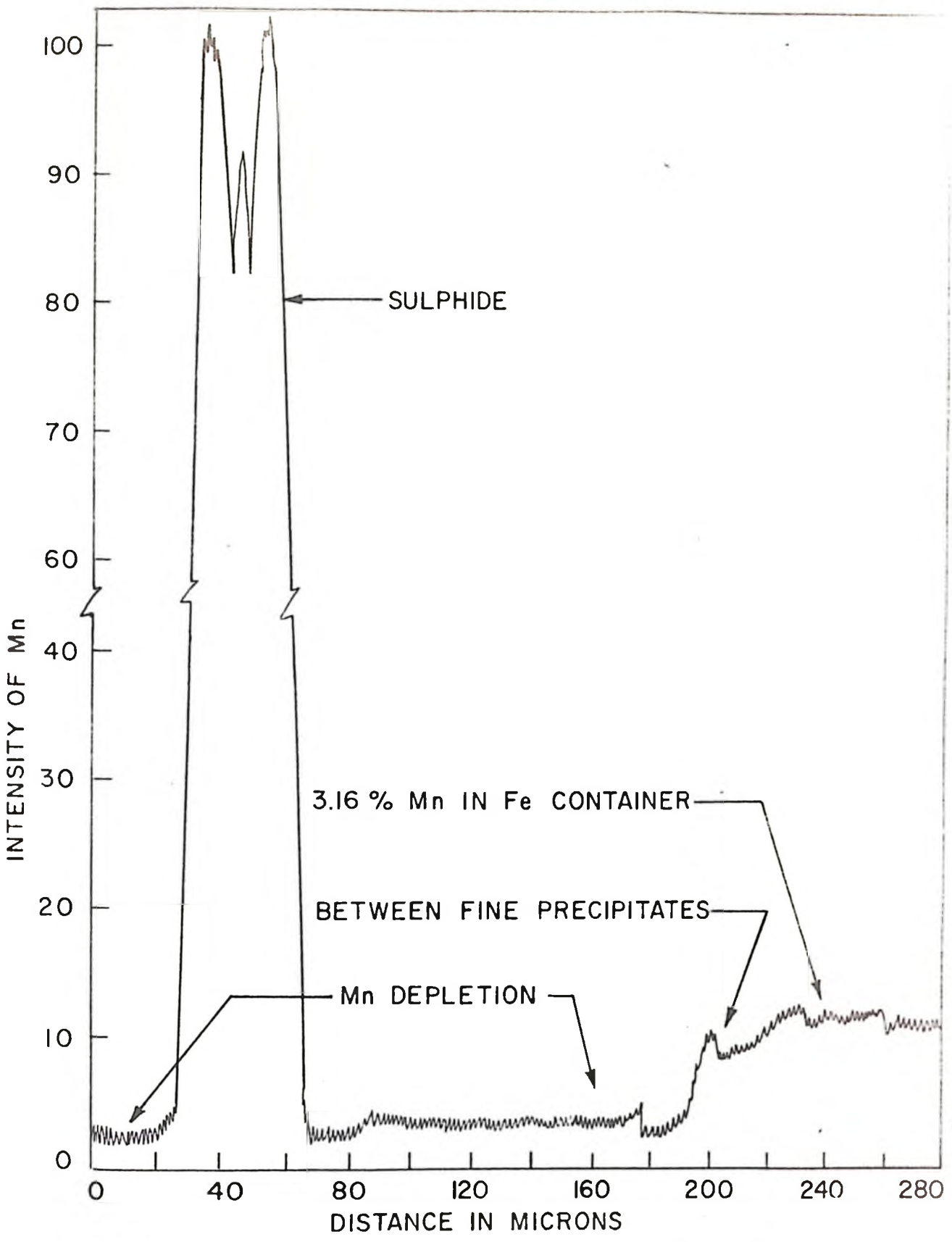

Fig. 38 A semi-schematic reproduction of a strip chart from the McMaster probe showing the X-ray intensity of $Mn_{K\alpha(3)}$ across the sulphide-iron interface of a diffusion couple.

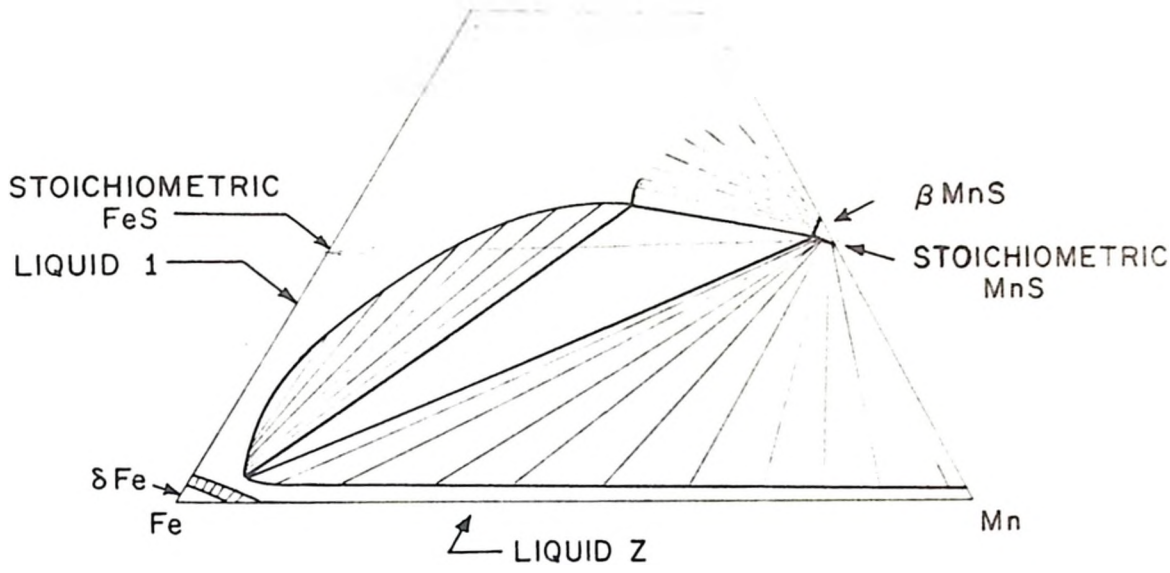

Fig. 39 Semi-schematic ternary isotherm in the system Fe-Mn-S just below the solidification point of iron (1535°C).

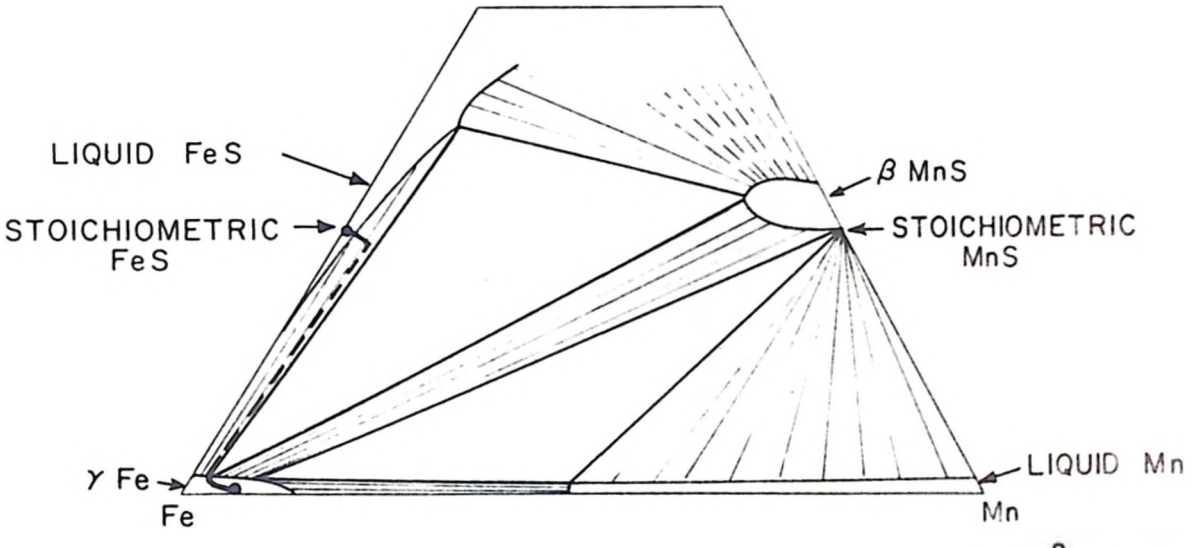

Fig. 40 Semi-schematic ternary isotherm in the system Fe-Mn-S at 1300°C. The diffusion path for the liquid FeS-Fe-3.16% Mn diffusion couple is indicated on the isotherm.

Table I Tabulation of Data on the Electron Probe

Probe	Take-off Angle	Lines Analysed	Accelerating Voltage	Background Measurement
McMaster	55°	(Mn and Fe) Kα(3)	25 to 30 K.V.	I_{Mn} on Fe
U. of T. (Philips)	15.5°	" Kα(5)	25 K.V.	I_{Fe} on Mn
Fisher (JXA-3A)	20°	" Kα(1)	25 K.V.	(all probes)

Table II Tabulation of Data on the Microanalysed Pots

Pot No.	Initial Mn/S	Container	Type of FeS Addition	Heat Treatment
1	1.54	Pure Iron	Commercial	1300°C for 80 minutes
4	0.63	" "	"	" " " "
5	0.30	" "	"	" " " "
8	0.43	Battelle iron	"	" " " "
10	0.40	" "	Levitated	" " " "

Table IIa Pot No. 1 Point Counting Data from the McMaster Probe

Microanalysis was done across a βMnS-αFeS interface. I'_A and I'_{100A} are the raw intensities, I_A and I_{100A} are intensities corrected for background. All intensities recorded are the average of several counting times on the same spot.

	Standards		αFeS			βMnS			αFe		
	I'_{100A} c.p.m	$I_{Background}$ c.p.m.	I'_A c.p.m.	$\frac{I_A}{I_{100A}}$	% A	I'_A c.p.m.	$\frac{I_A}{I_{100A}}$	% A	I'_A c.p.m.	$\frac{I_A}{I_{100A}}$	% A
Area 1 Mn	37,327	151				23,446	0.6266	64.1	2,227	0.0538	5.38
Fe	32,264	165				232	0.0021	0.2	31,132	0.9650	96.5
S											
Area 2 Mn	38,031	156				23,500	0.6160	63.4	2,250	0.0553	5.53
Fe	31,598	142				232	0.0028	0.3			
S								36.3			
Area 3 Mn	40,447	150				26,041	0.6420	66.0	2,354	0.0549	5.50
Fe	21,124	148				248	0.0048	.5	20,093	0.9520	95.2
S								33.5			

Table IIb Pot No. 4 Point Counting Data from the University of Toronto Probe

Microanalysis was done at the junction of three phases, αFeS, βMnS and αFe. I'_A and I'_{100A} are the raw intensities, I_A and I_{100A} are intensities corrected for background. All intensities recorded are the average of several counts on the same spot. The value for %Mn in αFe was determined by averaging the I'_A values from areas 1 to 5 and relating the average to I'_{100Mn} = 66,133. Only one spectrometer was available for counting. Spurious counts were detected at the time areas 6 and 7 were examined and further probing at the time was discontinued.

		Standards		αFeS			βMnS			αFe		
		I'_{100A} c.p. 10 sec.	$I_{Background}$ c.p. 10 sec.	I'_A c.p. 10 sec.	$\frac{I_A}{I_{100A}}$	% A	I'_A c.p. 10 sec.	$\frac{I_A}{I_{100A}}$	% A	I'_A c.p. 10 sec.	$\frac{I_A}{I_{100A}}$	% A
Area 1	Mn	66,133	102	1,984	0.0300	3.2	8,136	0.1217	12.6	153	0.0007	0.07
	Fe	77,957	167	39,951	0.5114	53.5	27,069	0.3458	36.2			
	S					43.3			51.2			
Area 2	Mn	as above	as above	3,308	0.0500	5.3	8,060	0.1205	12.5	159	0.0007	0.07
	Fe			37,295	0.4773	50.0	30,102	0.3848	40.0			
	S					44.7			47.5			
Area 3	Mn	as above	as above	2,494	0.0378	4.1	6,726	0.1003	10.5	153	0.0007	0.07
	Fe			37,037	0.4740	49.5	27,599	0.3526	36.7			
	S					46.4			52.8			
Area 4	Mn	as above	as above	1,873	0.0284	3.1	8,239	0.1232	13.0	143	0.0007	0.07
	Fe			39,403	0.5044	52.5	29,291	0.3744	39.0			
	S					44.4			48.0			

Table IIb (Continued)

	Standards		αFeS			βMnS			αFe		
	I'_{100A} c.p. 10 sec.	$I_{Background}$ c.p. 10 sec.	I'_A c.p. 10 sec.	$\frac{I_A}{I_{100A}}$	% A	I'_A c.p. 10 sec.	$\frac{I_A}{I_{100A}}$	% A	I'_A c.p. 10 sec.	$\frac{I_A}{I_{100A}}$	% A
Area 5 Mn Fe S	60,773 73,028	as above	2,003 40,474	0.0312 0.5519	3.5 57.8 38.7	9,419 29,818	0.1533 0.4060	16.0 42.5 41.5	137	0.0007	0.07
Area 6 Mn Fe S	76,740 88,048	223 298	3,920 41,700	0.0484 0.4720	5.0 51.1 43.9	8,950 35,600	0.1141 0.4021	12.3 43.3 44.4	225		not detected
Area 7 Mn Fe S	as above	as above	3,580 41,976	0.0439 0.4751	4.7 51.4 43.9	10,556 33,358	0.1350 0.3769	14.5 40.8 44.7	220		not detected

Table IIc Pot No. 5 Point Counting Data from the McMaster Probe

Microanalysis was done across a βMnS-αFe interface. I'_A and I'_{100A} are the raw intensities, I_A and I_{100A} are intensities corrected for background. All intensities recorded are the average of several counts on the same spot.

	Standards		αFeS			βMnS			αFe		
	I'_{100A} c.p.m.	$I_{Background}$ c.p.m.	I'_A c.p.m.	$\frac{I_A}{I_{100A}}$	% A	I'_A c.p.m.	$\frac{I_A}{I_{100A}}$	% A	I'_A c.p.m.	$\frac{I_A}{I_{100A}}$	% A
Area 1 Mn Fe S	77,284 41,630	245 210				35,703 8,121	0.4602 0.1910	47.4 19.4 33.2	644	0.0052	0.52
Area 2 Mn Fe S	as above	as above				37,476 6,832	0.4833 0.1599	49.5 16.3 34.2	696	0.0059	0.59
Area 3 Mn Fe S	74,643 38,488	245 210				35,011 7,151	0.4672 0.1813	47.5 18.5 34.0	676	0.0058	0.58
Area 4 Mn Fe S	as above	as above				35,680 6,717	0.4763 0.1700	49.0 17.3 33.7	683	0.0059	0.59

Table IId Pot No. 5 Point Counting Data for Mn on the University of Toronto Probe

Microanalysis was done at the junction of three phases, areas 1, 2 and 3 and at two phase interfaces, areas 4 and 5. I'_A and I'_{100A} are the raw intensities, I_A and I_{100A} are intensities corrected for background. All intensities recorded are the average of several counts on the same spot. Only one spectrometer was available for counting.

	Standards		αFeS			βMnS			αFe		
	I'_{100A} c.p. 10 sec.	$I_{Background}$ c.p. 10 sec.	I'_A c.p. 10 sec.	$\frac{I_A}{I_{100A}}$	% A	I'_A c.p. 10 sec.	$\frac{I_A}{I_{100A}}$	% A	I'_A c.p. 10 sec.	$\frac{I_A}{I_{100A}}$	% A
Area 1 Mn	89,245	131	3,333	0.0359	3.8	11,665	0.1294	14.0	231 (2,313/ 100 sec.)	0.00112	0.11
Area 2 Mn	87,388	131	3,465	0.0382	4.1	16,514	0.1878	20.4	238 (2,377/ 100 sec.)	0.0012	0.12
Area 3 Mn	89,737	131	3,300	0.0354	3.2	14,556	0.1610	17.4	233 (2,333/ 100 sec.)	0.0011	0.11
Area 4 Mn	89,281	131				33,080	0.3690	40.1	419 (4,186/ 100 sec.)	0.0032	0.32
Area 5 Mn	77,673	131				28,685	0.3682	40.0	216	0.0011	0.11

Table IIe Pot No. 8 Point Counting Data from the Fisher Probe

The area microanalysed was traversed by the line scan of Fig. 31 and is shown in the scanning images of Fig. 32. The values of Mn, Fe and S recorded in area 1 for βMnS actually correspond to a phase mixture of αFeS and βMnS. The values recorded at approximately 5μ intervals parallel to the line scan are given in spots 1 to 5. I'_A and I'_{100A} are the raw intensities, I_A and I_{100A} are the intensities corrected for background. All intensities were recorded over a 20 second interval.

		Standards		αFeS			βMnS			αFe		
		I'_{100A} c.p. 20 sec.	$I_{Background}$ c.p. 20 sec.	I'_A c.p. 20 sec.	$\frac{I_A}{I_{100A}}$	% A	I'_A c.p. 20 sec.	$\frac{I_A}{I_{100A}}$	% A	I'_A c.p. 20 sec.	$\frac{I_A}{I_{100A}}$	% A
Area 1	Mn	104,960	44	2,074	0.0194	2.0	21,264	0.2020	21.5	58		not detected
	Fe	112,284	91	48,186	0.4214	45.0	26,810	0.2382	24.8			
	S					53			53.7			
Spot 1	Mn						25,215	0.2399	25.9			
	Fe						23,818	0.2114	22.1			
	S								52.0			
Spot 2	Mn						32,532	0.3097	33.0			
	Fe						19,518	0.1732	18.1			
	S								48.9			
Spot 3	Mn						41,659	0.3967	42.5			
	Fe						12,575	0.1113	11.6			
	S								45.9			
Spot 4	Mn						45,997	0.4380	46.8			
	Fe						9,722	0.0858	8.8			
	S								44.4			
Spot 5	Mn						46,841	0.4460	47.5			
	Fe						9,432	0.0832	8.5			
	S								44.0			

Table IIf Pot No. 10 Point Counting Data from the Fisher Probe

The area microanalysed is shown in the scanning images of Fig. 33. The values of Mn, Fe and S recorded in area 1 for βMnS actually correspond to a phase mixture of αFeS and βMnS. Spot 1 was selected approximately in the center of the phase mixture and spot 2 was chosen in pure βMnS. Spot 3 was recorded in αFeS adjacent to the phase mixture. I'_A and I'_{100A} are the raw intensities, I_A and I_{100A} are the intensities corrected for background. All intensities were corrected over a 20 second interval.

		Standards		αFeS			βMnS			αFe		
		I'_{100A} c.p. 20 sec.	$I_{Background}$ c.p. 20 sec.	I'_A c.p. 20 sec.	$\frac{I_A}{I_{100A}}$	% A	I'_A c.p. 20 sec.	$\frac{I_A}{I_{100A}}$	% A	I'_A c.p. 20 sec.	$\frac{I_A}{I_{100A}}$	% A
Area 1	Mn	111,071	41	124	0.0007	0.07	39,362	0.3542	38.0	73	0.0003	.03
	Fe	106,737	89	51,795	0.4749	49.8	11,860	0.1081	11.2			
	S								50.8			
Spot 1	Mn	as above	as above				45,076	0.4083	43.5			
	Fe						8,883	0.0835	8.5			
	S								48.0			
Spot 2	Mn	as above	as above				46,211	0.4158	44.3			
	Fe	108,885					10,525	0.0959	9.8			
	S								45.9			
Spot 3	Mn	as above	as above	133	0.0008	0.08						
	Fe	106,203		48,825	0.4580	48.0						
	S					51.9						

Table III Couple No. 6 Point Counting Data from the University of Toronto Probe

The areas microanalysed were all at the intersections of the three phases, αFeS, βMnS and αFe. However, because the size of the electron beam (about 2 μ) was not much smaller than the extent of the sulphide phases, positioning of the beam entirely on one phase was difficult. Also, iron precipitates or fingers in the sulphide may have contributed to the iron intensities. I'_A and I'_{100A} are the raw intensities, I_A and I_{100A} are intensities corrected for background. All intensities are the average of several counting times on the same spot. Only one spectrometer was available.

		Standards		αFeS			βMnS			αFe		
		I'_{100A} c.p. 10 sec.	$I_{Background}$ c.p. 10 sec.	I'_A c.p. 10 sec.	$\frac{I_A}{I_{100A}}$	% A	I'_A c.p. 10 sec.	$\frac{I_A}{I_{100A}}$	% A	I'_A c.p. 10 sec.	$\frac{I_A}{I_{100A}}$	% A
Area 1	Mn	72,500	106	2,280	0.030	3.5	17,700	0.243	26.4	250	0.0020	0.20
	Fe	76,000	173	41,100	0.540	58.5	71,904	0.314	34.0			
	S					38.0			39.6			
Area 2	Mn	as above	as above	2,090	0.027	2.9	23,200	0.318	34.5	220	0.0016	0.16
	Fe			44,200	0.581	62.0	18,650	0.244	26.4			
	S					35.1			39.1			
Area 3	Mn			2,060	0.027	2.9	14,850	0.204	22.0	not counted		
	Fe			44,700	0.588	62.5	31,300	0.411	44.5			
	S					34.6			33.5			
Area 4	Mn			2,340	0.0309	3.3	12,650	0.173	18.8	not counted		
	Fe			41,000	0.539	58.1	29,350	0.385	41.5			
	S					38.6			39.7			